*J. Fluid Mech.* (2020), *vol*. 901, A11. © The Author(s), 2020.
Published by Cambridge University Press
doi:10.1017/jfm.2020.514



# Effect of the dynamic slip boundary condition on the near-wall turbulent boundary layer

**Cong Wang**[1] **and Morteza Gharib** [1,†]

[1]Division of Engineering and Applied Science, California Institute of Technology, Pasadena, CA 91125, USA

(Received 3 November 2019; revised 11 May 2020; accepted 13 June 2020)

The manipulation of near-wall turbulent structures in a turbulent boundary layer (TBL) is an effective way to reduce the turbulent frictional drag. This paper demonstrates the effectiveness of a novel approach for the manipulation of near-wall structures in a TBL with Reynolds number ($Re_\theta$) set to 1200. The manipulation is achieved by employing a sustainable wall-attached air-film array. The static and dynamic interface configuration of the air film can be modulated, which generates a dynamic slip boundary condition. For modulation frequencies within the TBL receptivity, this approach shows that it can effectively modify the TBL near-wall velocity/vorticity field. For a typical modulation frequency of 50 Hz, the near-wall mean streamwise velocity decreases and the wall-normal velocity increases when compared to the canonical flat plate TBL. The mean transverse vorticity is suppressed in the near-wall region and its peak is 'pushed' outward away from the wall. In the vicinity of modulated air-film array, the phase-locked velocity/vorticity field demonstrates harmonic motions such as a Stokes-type oscillatory motion. The distribution of shear stresses indicates suppressed momentum transfer toward the wall. Estimation of the wall skin friction via the Clauser chart method indicates a reduction of the wall skin friction up to 40 % in the downstream region of the air-film array. A control volume analysis shows that the TBL gains a significant amount of momentum over the oscillating air films, which suggests that the oscillating air film acts like a source of momentum. This pumping effect could potentially explain the observed wall skin friction reduction effect.

**Key words:** turbulence control, turbulent boundary layers, drag reduction

## 1. Introduction

The presence of turbulent boundary layers (TBLs) is a significant source of energy loss in many engineering applications. For example, Fukuda *et al.* (2000) reported that hydrodynamic frictional drag is responsible for up to 80 % of the total energy consumption of naval vessels such as oil tankers. In this respect, many previous research studies have focused on suppressing wall skin friction by manipulating the TBL. For example, it has been demonstrated that the local wall skin friction can be significantly reduced by injecting elastic additives such as polymers or micro-bubbles into the TBL (White & Mungal 2008; Ceccio 2010). The underlying reason points to the interactions between the turbulent flow

† Email address for correspondence: mgharib@caltech.edu

and elastic agents modifying the shear-generating structures of TBLs. Another promising method is to passively induce slip flow by maintaining a layer of low-viscosity air or oil at the wall by employing super-hydrophobic surfaces (Choi & Kim 2006) or oil-infused surfaces (Rosenberg *et al.* 2016). The low-viscosity fluids perform the role of a lubricating layer, which allows the turbulent flow to 'slip' over the surface. The slip velocity offsets the shear strain rate and thus reduces the wall friction. Besides the slippage effect, the pressure coupling effect between super-hydrophobic surface and TBL is recently explored (Seo, García-Mayoral & Mani 2015). Reviews on using super-hydrophobic surfaces for drag reduction have been published in Rothstein (2010) and Golovin *et al.* (2016).

Although promising results were obtained with the aforementioned methods, their practical application to naval vessels is limited by several challenges. The method involving the ejection of elastic agents gives rise to environmental concerns and the injection and maintenance requirement for elastic agents diminishes their application potential for drag reduction. With regard to the passive slip-flow inducing method, detachment of the lubricating fluids in the turbulent flow prevents its usability (Rothstein 2010). The air or oil entrapped in the surface could be lost as the result of diffusion, turbulence fluctuations and wall shear stress (Choi & Kim 2006; Rothstein 2010). The loss of the lubrication layer could result in increased drag (Bidkar *et al.* 2014). Recently, the competition between the effect of drag reduction and drag increase over super-hydrophobic surfaces has been investigated (Rastegari & Akhavan 2015; Ling *et al.* 2016).

Here, we introduce a novel air-retaining system that can potentially address the above-mentioned limitations and effectively manipulate the near-wall TBL. A schematic drawing of the concept is shown in figure 1, in which two distinct features are represented. The first feature is a dense distribution of close-packed surface dimples (i.e. square-shape dimples) that act as air pockets. The inner surface of these dimples is selectively coated with super-hydrophobic material (represented by the stripes in figure 1) while the outside surface remains super-hydrophilic. Owing to the sharp wettability gradient between the inner and outer surface of dimples, air–water interfaces will form at the edges of surface dimple as wall-attached air films when the surface dimples are immersed in water. This design suppresses the tendency of the air films to connect to neighbouring air films. In this way, the stability of wall-attached air films is enhanced by the surface tension effect because of the small size of each air film.

The second feature is a pressure controlled air chamber, which is commonly connected to each surface dimple. This feature enables air to be replenished in the case of occasional air loss due to severe turbulence and/or prolonged air diffusion at the air–water interface. In addition, the air-film curvature can be controlled by regulating the air-chamber pressure. The concavity of the air-film interface can be adjusted to be flat, concave (sagging into the dimple) or convex (bulging out into the TBL), depending on the static pressure of the air chamber. Dynamic control of the air-chamber pressure is also possible by incorporating a pressure source. In this study, speakers are used to produce the desired dynamic pressure to modulate the dynamic oscillation of the air films. Because of the common air-chamber design, the modulated air films oscillate in phase; however, their dynamic oscillation also depends on the local fluctuations in the TBL. The two features of the proposed system essentially generate a dynamic slip boundary condition. This paper demonstrates that the near-wall TBL can be effectively manipulated by this boundary condition.

The remainder of this paper is organized as follows. Section 2 demonstrates the experimental set-up. In § 3 the interaction between the TBL is qualitatively shown and the technique of phase average is introduced. After that, the quantitatively mapped velocity/vorticity field of the TBL and an analysis of the streamwise momentum transfer

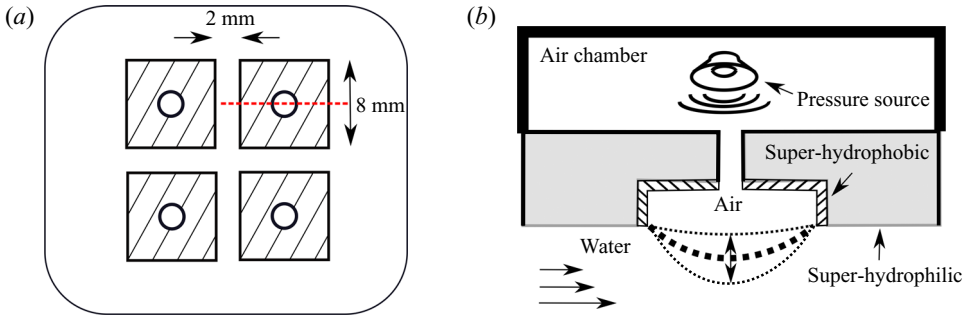


FIGURE 1. Schematic of the (*a*) bottom view and (*b*) cross-sectional view of the proposed system (along the dashed line in (*a*)) to illustrate the formation of a wall-attached air film by creating a square array of surface dimples and patterning their surface wettability. The stripes represent the super-hydrophobic surface inside the surface dimple. In the cross-sectional view, the air film is pinned to the edge of the surface dimple and is represented by the black dotted line. The surface dimples are connected to a common air chamber, which incorporates the dynamic pressure source. This design enables the static configuration and dynamic oscillation of the air-film array to be controlled for the purpose of manipulating the TBL.

process is presented in § 4. The estimated wall skin friction reduction effect is also shown. In § 5, potential physical mechanisms of the aforementioned observations are discussed. Finally, the conclusions and potential future work is presented in § 6.

## 2. Experimental set-up

The experiments were conducted in the free surface water channel at the California Institute of Technology. The test section of the water channel is 2 m long, 1 m wide and 1 m deep, with the free-stream turbulent intensity below 0.1 %. The TBL was generated over a 0.5 m (W) × 1.8 m (L) flat plate, as shown by the schematic illustration of the model in figure 2. The flow is from left to right and the velocity components ($u$, $v$, $w$) are along the streamwise ($x$), wall-normal ($y$) and transverse ($z$) directions, respectively. Because the test section is wider than the flat plate, the plate is sandwiched between two sidewalls to avoid any potential transverse flow. The water level in the water channel was set to 0.4 m and the flat plate was immersed 0.1 m below the free surface, leaving 0.3 m deep water beneath it. The air-film retaining system was fitted into the central opening area of the flat plate unit with the air films facing downward. This orientation retained the wall-attached air films more effectively by virtue of the buoyancy force. The canonical flat plate TBL (baseline case) was recovered by replacing the air-retaining system with a smooth flat surface that fit flush against the flat plate. The TBL was tripped by a 1 mm thick, 4 mm wide trip wire attached at the leading elliptical edge of the flat plate. A trailing flap was attached to the flat plate and its angle was carefully adjusted to eliminate the pressure gradient in the TBL. The magnitude of the free-stream acceleration factor ($K = (\partial U_\infty/\partial x)(\nu/U_\infty^2)$, where $U_\infty$ is the free-stream velocity and $\nu$ is the kinematic viscosity of water) was approximately $1 \times 10^{-7}$, indicating that the baseline TBL has no pressure gradient (De Graaff & Eaton 2000).

The baseline TBL parameters are listed in table 1. The Reynolds number based on momentum thickness ($Re_\theta = U_\infty\theta/\nu$) was 1200, where $\theta$ is the momentum thickness of the TBL. The friction velocity $u_{\tau 0}$, which was calculated using the Clauser chart method

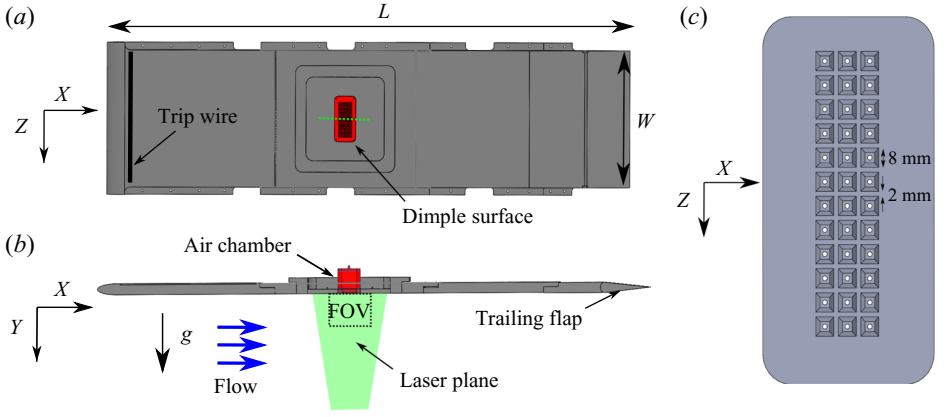


FIGURE 2. Schematic of the experimental set-up (*a*) bottom view, (*b*) cross-sectional view and (*c*) the dimple (air-pocket) surface. The coordinate system and direction of the gravitational acceleration are shown. The laser plane along the central line of the flat plate is highlighted in green colour. The dimple surface and air chamber are highlighted in red colour. The dimensions of the dimple array and that of a surface dimple are given in (*c*). FOV, field of view.

| $U_\infty$ | $\delta_0$ | $u_{\tau 0}$ | $\dfrac{\nu}{u_{\tau 0}}$ | $Re_\theta$ | $Re_\tau$ |
|---|---|---|---|---|---|
| (m s$^{-1}$) | (mm) | (m s$^{-1}$) | (mm) | — | — |
| 0.438 | 23.5 | 0.020 | 0.046 | 1200 | 470 |

TABLE 1. The parameters of the baseline TBL.

(Clauser 1954), was 0.020 m s$^{-1}$. The TBL inner length scale ($\nu/u_{\tau 0}$) and the friction Reynolds number ($Re_\tau = u_{\tau 0}\delta_0/\nu$) are also shown.

The surface dimple array consisted of 12 × 3 surface dimples, which spanned 120 mm in the transverse direction and 30 mm in the streamwise direction. The dimensions of the surface dimple are shown in the enlargement within figure 2. As illustrated, 8 mm-sized square dimples were spaced at equal distances from each other with a 2 mm gap in between. The wall-attached air films covered 80 % of the total surface. The air films were selectively maintained as passive flat, passive bulged or bulged with modulation. The modulation frequency $f$ was selected based on the intrinsic frequencies of the baseline TBL. There are two intrinsic frequencies that can be defined, $U_\infty/\delta_0$ and $u_{\tau 0}^2/\nu$, which are associated with the largest and smallest eddies in TBL, respectively. The values of the two frequencies are 18 and 434 Hz in the current study. The modulation frequency is selected within the range defined by the two values to allow the oscillating air films to interact with certain turbulent eddies. A frequency of 50 Hz was selected because a strong air-film response was observed at this frequency. With the current air-pocket dimensions, the Helmholtz resonance frequency of the cavity is 9.3 KHz, which is much higher than the air-film modulation frequency. As such, the frequency dependence of air-film oscillation is unlikely due to the Helmholtz resonance inside the air-pocket cavity. Instead, it could be connected to the Bessel drum oscillation mode that is excited by the modulation. The

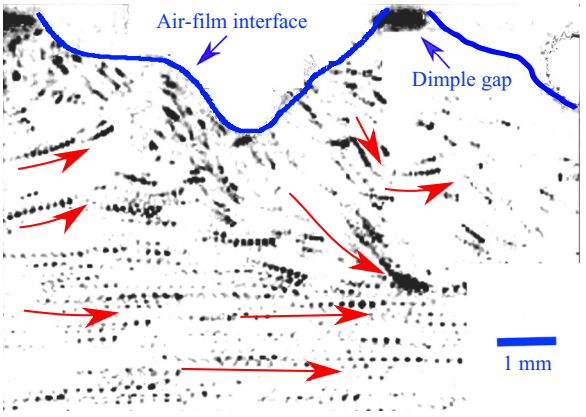


FIGURE 3. Particle trajectories near the bulged air films modulated at 50 Hz demonstrating strong wall-normal motion. The flow is from left to right and the air-film interface is highlighted by the blue curve. Particle trajectories are generated by overlaying particle images captured in a period of 0.01 s (equivalent to a half-modulation cycle).

non-dimensional modulation frequency $f^+ = f\nu/u_{\tau 0}^2$ has a value of 0.125. The results of additional test cases can be found in Wang (2019).

The flow field was measured using digital particle image velocimetry (DPIV). The water was uniformly seeded with neutrally buoyant silver coated particles of 13 μm in diameter (Potters Industries LLC). A 6 Watt continuous green laser sheet illuminated the flow in the plane normal to the wall ($x$–$y$ plane) along the central line of the flat plate. A high-speed camera (IDT camera Y7 model) recorded 25 000 particle images at 1500 frames per second for each measurement. The flow field in the surrounding region of the air-film array was measured, which included both the upstream and downstream regions of the air-film array. Because of the limited size of the field of view of the camera, multiple DPIV measurements were carried out at different streamwise locations and assembled to form the final field of view which enclosed the region occupied by the air-film array. The streamwise and wall-normal locations of the points of interest (denoted as $x_0^+$ and $y_0^+$) are in the wall unit of the baseline TBL (i.e. $x_0^+ = xu_{\tau 0}/\nu$).

## 3. Qualitative results and phase-average technique

An example of the effects of the oscillating air film on the near-wall TBL is depicted in figure 3, which shows the particle trajectories in the vicinity of bulged air films that are modulated at 50 Hz. The particle trajectory is achieved by overlaying particle images over 0.01 s (equivalent to one half-modulation cycle). Figure 3 shows that the particles near the air films did not move parallel to the free stream. Instead, strong wall-normal flow motion presented in the near-wall region. The air-film interface curvature was locally distorted by the coupled air-film/TBL interaction. In the case of the passive flat air film, these strong wall-normal flow motions were not visible.

The wall-attached air films oscillated with and without dynamic modulation. Figure 4 shows the time series of air-film interface oscillation for a passive flat air film, passive bulged air film and bulged air film modulated at 50 Hz, respectively. The oscillating air film is occasionally invisible because of the lack of scattered light. To improve the effect of visualization, the air-film interfaces are highlighted using red lines. In the cases of passive

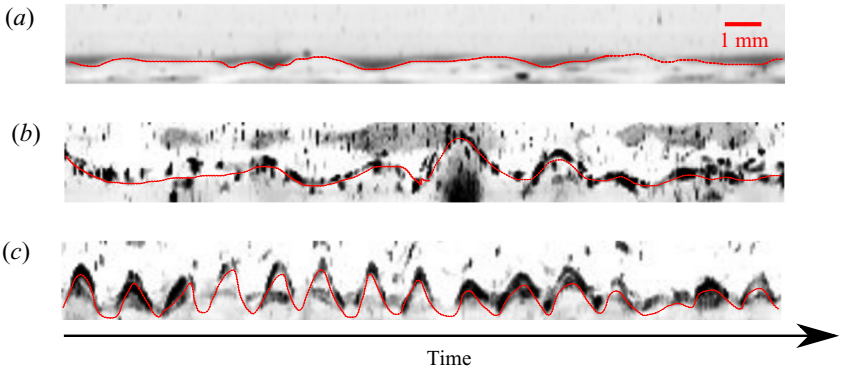


FIGURE 4. Air-film interface wall-normal oscillation time series tracked over 0.3 s in the presence of (*a*) passive flat air film, (*b*) passive bulged air film and (*c*) bulged air film modulated at 50 Hz. With 50 Hz modulation, the air-film oscillation demonstrates a strong 50 Hz component.

| Air-film oscillation range | Flat air film | Bulged air film | Bulged air film modulated at 50 Hz |
|---|---|---|---|
| $h$ (mm) | 0–0.28 | 1.41–2.80 | 1.3–2.78 |
| $h_0^+ \left(\frac{\nu}{u_{\tau 0}}\right)$ | 0–6 | 31–61 | 28–60 |

TABLE 2. Range of the maximum height of the air film when it is maintained passive flat, passive bulged and bulged with modulation at 50 Hz.

flat and bulged air film, the air-film interface oscillates at random frequencies. However, in the presence of 50 Hz modulation, the air-film interface oscillation is dominated by a single frequency component. The maximum height ($h$) of the air films is selected to represent the general oscillation behaviour of air-film array. The peak-to-peak oscillation amplitude of $h$ seems to depend on the static configuration of the air film. Table 2 lists the range of $h$ in both the physical unit (i.e. millimetres) and the baseline wall unit (i.e. $h_0^+ = hu_{\tau 0}/\nu$). When the air film is maintained passively flat, its oscillation amplitude is small. For the bulged air film with and without modulation, the oscillation amplitudes are much larger. In the cases of passive or modulated bulged air film, $h_0^+$ could exceed 30, which indicates that the air films may directly interact with the TBL log region. No air-film depletion was observed in all three test cases.

The air-film oscillation time series shown in figure 4 reveals the dynamic behaviour of the near-wall TBL. For all cases presented here, any flow quantity ($g$) can be Reynolds decomposed to a time-averaged component and a fluctuating component, i.e. $g = \overline{G} + g''$. Particularly, in the presence of periodic modulation, $g$ can be conveniently decomposed into three components

$$g = \overline{G} + \tilde{G} + g', \tag{3.1}$$

where $\tilde{G}$ is phase locked to the periodic oscillation of the air film. Therefore, $\tilde{G}$ periodically varies in a modulation cycle. This decomposition approach is often known as triple

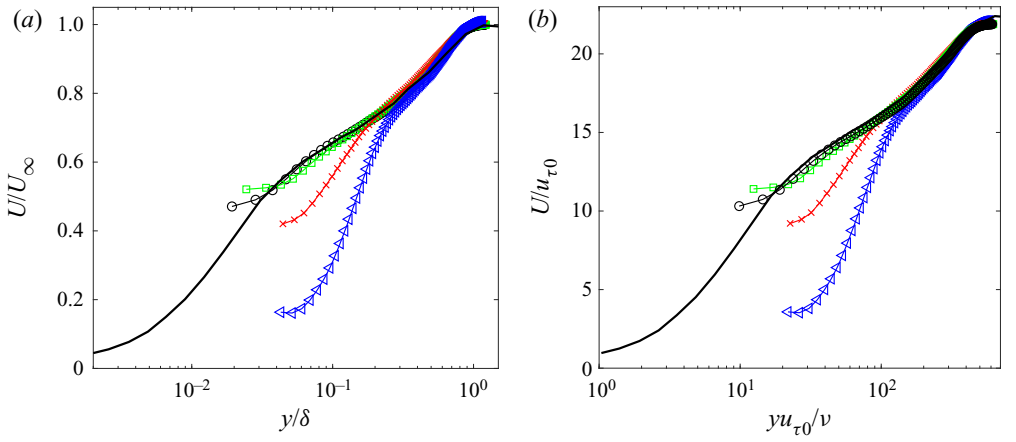


FIGURE 5. Mean streamwise velocity profiles measured at $x_0^+ = 1400$ and non-dimensionalized by (*a*) outer scale and (*b*) inner scale of the baseline TBL. The air-film array is located between $x_0^+ = 900$ and $x_0^+ = 1500$. Symbols: triangles, bulged air film modulated at 50 Hz; crosses, bulged air film; squares, flat air film; circles, baseline TBL; solid line, TBL with $Re_\theta = 1430$ (De Graaff & Eaton 2000).

decomposition (Hussain & Reynolds 1970), which enables the periodic component of the flow field such as the phase-averaged quantity $(\overline{G} + \tilde{G})$ to be analysed more distinctly.

## 4. Behaviour of the velocity and vorticity field

In this section, the mean velocity and vorticity fields in the vicinity of the air films are shown when the air films are subject to various control conditions. In the case of modulation, the phase-averaged velocity/vorticity field is also demonstrated. Afterwards, the shear stress components are presented, which provides insight into the process of transferring the streamwise momentum. Lastly, an estimation of the wall skin friction in the surrounding region of the air-film array is provided.

### 4.1. *Mean velocity and vorticity field*

#### 4.1.1. *Mean streamwise velocity ($\overline{U}$)*

The profiles of mean streamwise velocity ($\overline{U}$) are compared in figures 5(*a*) and 5(*b*), in the presence of passive flat, passive bulged and bulged with 50 Hz modulation air-film array. The velocity profiles were non-dimensionalized by the outer scale ($\delta_0$ and $U_\infty$) or the inner scale ($\nu/u_{\tau 0}$ and $u_{\tau 0}$) of the baseline case. The air-film array is located between $x_0^+ = 900$ and $x_0^+ = 1500$ and the profiles are measured at $x_0^+ = 1400$. For reference purposes, the profile of the baseline TBL as well as the published literature hot-wire measurement at $Re_\theta = 1430$ (De Graaff & Eaton 2000) are also shown. In the case of bulged air film modulated at 50 Hz, the near-wall $\overline{U}$ is significantly reduced and the slope of the log region increases. The profile of the passive bulged air film exhibits similar changes but the degree of modification is less than that in the case with modulation. In contrast, the profile of the passive flat air film closely approximates that of the baseline case.

Both dynamic oscillation and free-slip boundary condition could contribute to the modification in $\overline{U}$. The free-slip boundary condition allows a slip velocity ($u_s$) at the air–water interface, which offsets the mean velocity profile. The slip velocity is defined

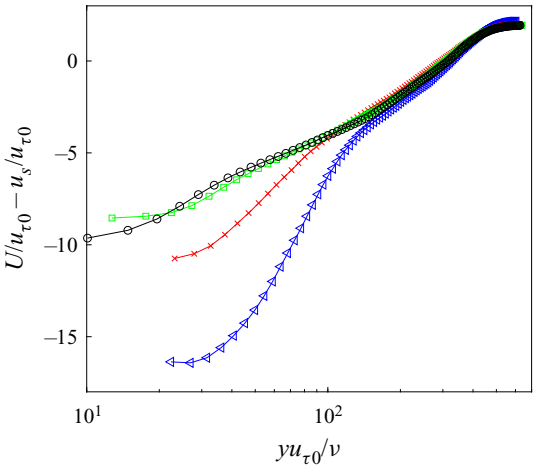


FIGURE 6. The mean velocity profiles shown in figure 5(*b*) offset by a slip velocity ($u_s^+ = 19.95$). Symbols: triangles, bulged air film modulated at 50 Hz; crosses, bulged air film; squares, flat air film; circles, baseline TBL.

as the product of the effective slip length $b$ and the wall-normal derivative of the mean velocity profile $\partial\overline{U}/\partial n$, i.e. $u_s = b(\partial\overline{U}/\partial n)$. Seo & Mani (2016) found that, over a patterned free-slip/no-slip flat surface, the slip velocity scales with the size of the surface texture, following a given scaling law. In our current experiment, the texture size $T$ is 10 mm, which has a non-dimensional value of $T^+ = 222$. The scaling relation proposed by Seo & Mani (2016) would predict the value of non-dimensional slip velocity ($u_s/u_{\tau 0}$) to be 19.95. The profiles of $\overline{U}$ would collapse after the slip velocity is subtracted. However, as shown in figure 6, the profiles of $\overline{U}/u_{\tau 0} - u_s/u_{\tau 0}$ do not collapse in the near-wall region. This observation could be due to the dominant effect of air-film dynamic oscillation or the effective slip length $b$ being modified. The dynamic oscillation seems to couple with the free-slip boundary condition. As such, a more appropriate scaling quantity, such as an effective dynamic slip velocity, is required.

The streamwise variation of $\overline{U}$ in the case of bulged air films modulated at 50 Hz is depicted in figure 7. The sample $\overline{U}$ profiles, with their streamwise locations shown along the top $x$-axis of figure 7, span from the upstream to the downstream region of the air-film array. In the upstream region of the air-film array (i.e. at $x_0^+ = 400$), $\overline{U}$ is similar to the baseline case. In the region occupied by the air-film array (i.e. at $x_0^+ = 1200$), the near-wall $\overline{U}$ is significantly reduced. In the downstream region of the air-film array (i.e. at $x_0^+ = 2000, 2400, 2800$), $\overline{U}$ gradually relaxes to the baseline case. A log-parallel layer, which is shown by the log-parallel black dashed lines in figure 7, was found to exist in the regions surrounding the air-film array but not over the air-film array. The downstream relaxing log-parallel layer indicates the presence of a re-developed log region.

### 4.1.2. *Mean wall-normal velocity ($\overline{V}$)*

The mean wall-normal velocity ($\overline{V}/u_{\tau 0}$) in the vicinity of the air films is compared to the baseline case in figure 8. The contour orientation is rotated by 180° relative to the physical orientation. Therefore, the air films (represented by green half-ovals) are located along the bottom edge of the contours. To avoid potential data discontinuity owing to the assembled final fields of view, the data at the overlapping edge for each individual field of view are discarded. The magnitude of $\overline{V}$ can be large in the presence of oscillating

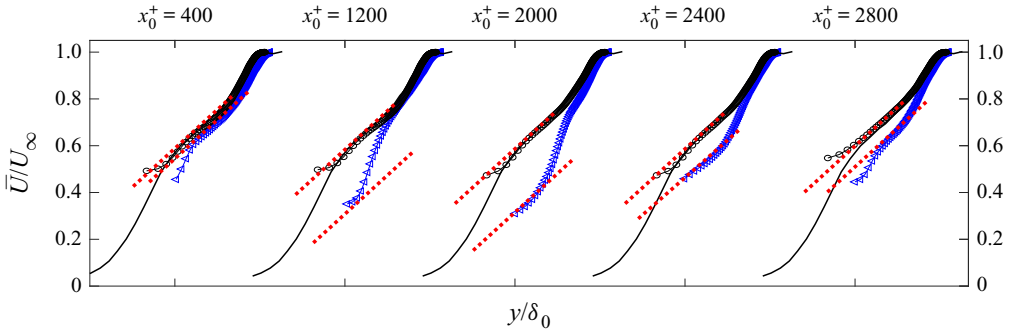


FIGURE 7. Streamwise variation of the profile of $\overline{U}$ in the presence of bulged air film modulated at 50 Hz. The streamwise locations are shown along the top $x$-axis. The air-film array is located between $x_0^+ = 900$ and $x_0^+ = 1500$. Log-parallel layers (indicated by red dotted lines) exist in the upstream and downstream regions of the air-film array but not over the air-film array. Symbols: triangles, bulged air film with 50 Hz modulation; circles, baseline TBL; The solid lines are the profiles of TBL with $Re_\theta = 1430$ obtained from De Graaff & Eaton (2000).

air films, although it is trivial in the baseline case. With 50 Hz modulation (shown in figure 8*a*), positive $\overline{V}$ is observed at the leading edge of air-film array and negative $\overline{V}$ exits in most regions downstream of the air-film array. The $\overline{V}$ is strong in the near-wall region, which resembles a blow and suction process at the wall. Similar behaviour is also found in the vicinity of passive bulged air films (shown in figure 8*b*). However, this phenomenon is invisible over passive flat air films (shown in figure 8*c*). The magnitude of baseline $\overline{V}$ (shown in figure 8*d*) is 20 times smaller than that shown in figures 8(*a*) and 8(*b*).

#### 4.1.3. *Mean transverse vorticity ($\overline{\Omega_z}$)*

The near-wall vortical structure is known to be critical for the self-sustainability of the TBL (Jiménez & Pinelli 1999). As the largest component of the vorticity field in the TBL, the mean transverse vorticity ($\overline{\Omega_z} = \partial\overline{V}/\partial x - \partial\overline{U}/\partial y$) deserves attention. Figure 9 compares $\nu\overline{\Omega_z}/u_{\tau 0}^2$ in the vicinity of the air films with that of the baseline case. For the convenience of viewing the vorticity distribution in the near-wall region, the wall-normal axis is set in log scale. The very near-wall region (i.e. below $y_0^+ = 30$) is excluded from the contour plot because of the poor DPIV accuracy in this area. When the 50 Hz modulation was used, $\overline{\Omega_z}$ (shown in figure 9*a*) is enhanced in the near-wall region upstream of the air-film array. In the region occupied by the air-film array, the peak of $\overline{\Omega_z}$ is observed to be 'pushed' outward away from the wall. At the trailing edge of the air-film array (at $x_0^+ = 1500$), the peak of $\overline{\Omega_z}$ is located at $y_0^+ = 70$, which is even above the maximum height of the air films ($h_0^+$). Together with the outward shift of $\overline{\Omega_z}$, the magnitude of $\overline{\Omega_z}$ is reduced in the near-wall region. Downstream of the air-film array, the thickened vorticity layer relaxes to the level of the baseline case. With the passive bulged air films (shown in figure 9*b*), $\overline{\Omega_z}$ is similarly 'pushed away' from the wall over the air films and relaxes in the downstream region. With passive flat air film (shown in figure 9*c*), $\overline{\Omega_z}$ is not 'pushed away' from the wall over the air-film array.

### 4.2. *Phase-averaged velocity and vorticity field*

In the case with modulation, the phase-averaged velocity/vorticity field is analysed. The profiles of phase-averaged streamwise velocity ($\overline{U} + \tilde{U}$) near the leading and trailing edges

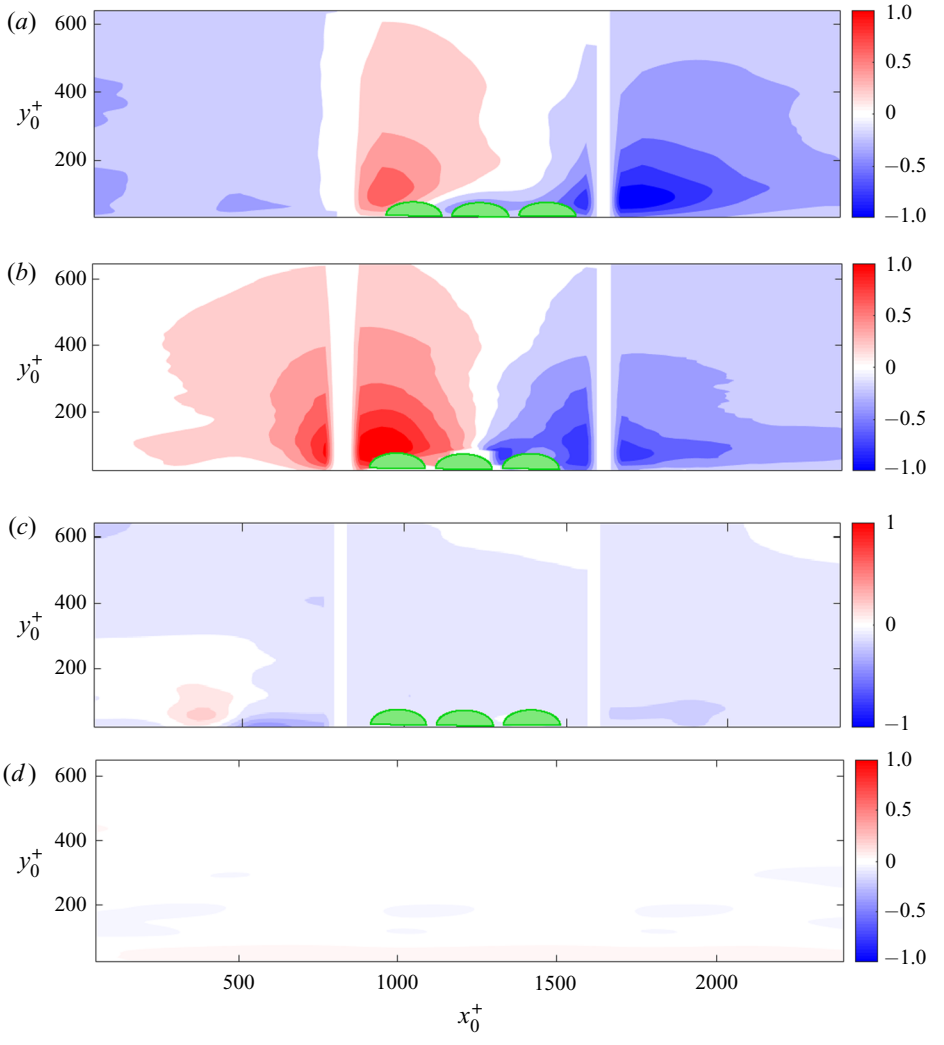


FIGURE 8. Contour of the mean wall-normal velocity ($\overline{V}/u_{\tau 0}$) in the case of (*a*) bulged air film modulated at 50 Hz, (*b*) passive bulged air film, (*c*) passive flat air film and (*d*) baseline TBL. The contours are rotated by 180° relative to the actual physical orientation. The air-film array is located between $x_0^+ = 900$ and $x_0^+ = 1500$ and is represented by green half-ovals along the bottom edge of the contours.

of the air-film array (i.e. at $x_0^+ = 800$ and $x_0^+ = 1550$, respectively) are first examined. Because $\overline{U} + \tilde{U}$ is phase-dependent even in the outer part of TBL, the associated length and velocity scales may be phase dependent as well. As such, a free-stream velocity ($U_e$) and boundary layer thickness ($\delta$) can be defined at each phase following the definition of TBL free-stream velocity and boundary layer thickness. The $\overline{U} + \tilde{U}$ profiles are non-dimensionalized by the phase-dependent outer scale. Figure 10 shows the profile of the maximum/minimum $(\overline{U} + \tilde{U})/U_e$ in one modulation cycle, which marks the oscillation range of phase-averaged streamwise velocity. The averaged profile $\overline{U}/U_e$ is also shown. The oscillatory motion was found to be mainly concentrated in the near-wall

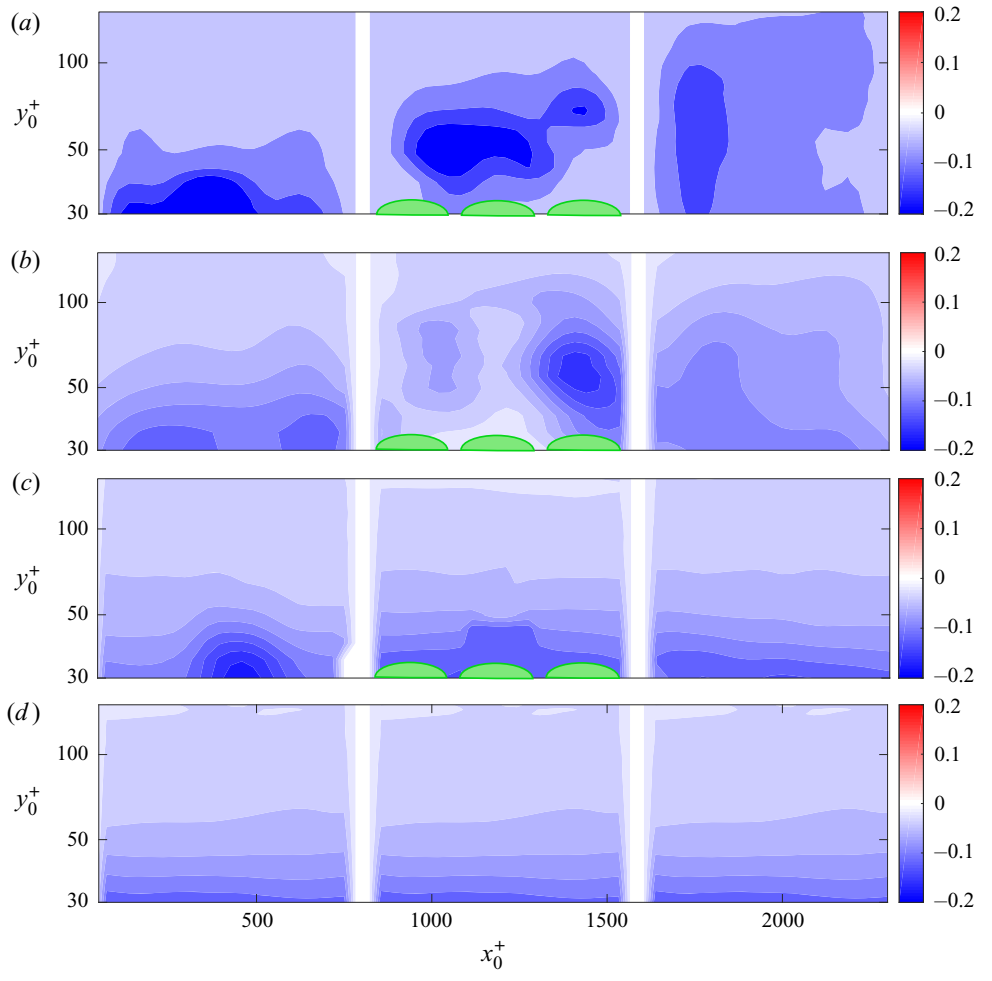


FIGURE 9. Mean transverse vorticity ($\nu\overline{\Omega_z}/u_{\tau 0}^2$) in the case of (*a*) bulged air film modulated at 50 Hz, (*b*) passive bulged air film, (*c*) passive flat air film and (*d*) baseline TBL. The air-film array is located between $x_0^+ = 900$ and $x_0^+ = 1500$ and is represented by green half-ovals along the bottom edge of contours. The $y$-axis is in log scale. To ensure data accuracy, only data above $y_0^+ = 30$ are shown; $\overline{\Omega_z}$ is 'pushed away' from the wall over the passive/modulated bulged air-film array and relaxes in the downstream region.

region. The value of $\overline{U} + \tilde{U}$ oscillates up to 10 % of the local mean velocity $\overline{U}$ in the near-wall region and 4 % in regions far away from the wall (i.e. at $y = 1.3\delta$). The shape of the mean profile $\overline{U}$ is modified. At the leading edge of the air-film array, $\overline{U}$ is slightly reduced relative to that of the baseline case in the region with wall-normal distance between 0.2 $\delta$ and 0.6 $\delta$. At the trailing edge of the air-film array, $\overline{U}$ is substantially reduced in the near-wall region below 0.2 $\delta$ but slightly increased in the region between 0.2 $\delta$ and 0.6 $\delta$.

The profiles of the phase-locked velocity component $\tilde{U}$ (non-dimensionalized by $u_{\tau 0}$) are shown in figure 11. The motion resembles that of the Stokes boundary layer, which is generated by a flat plate oscillating in the streamwise direction (Batchelor 2000). The

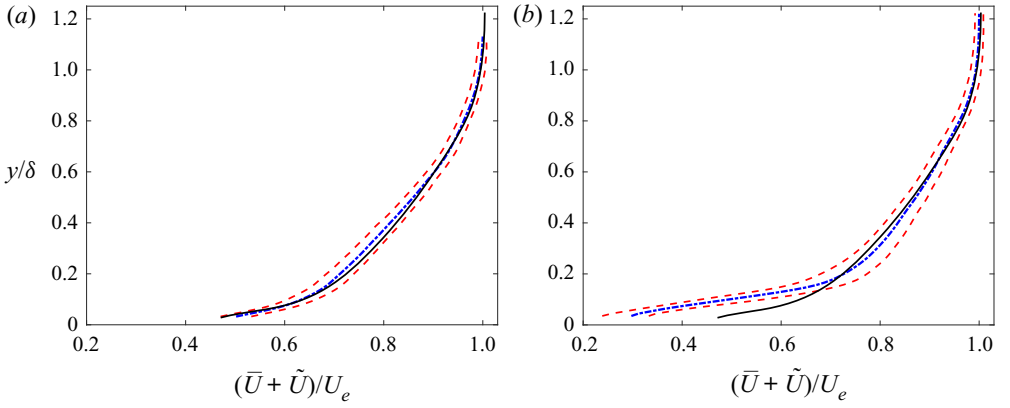


FIGURE 10. Profile of $(\overline{U}+\tilde{U})/U_e$ showing the oscillation range of phase-averaged streamwise velocity at the (*a*) leading edge ($x_0^+ = 800$) and (*b*) trailing edge ($x_0^+ = 1550$) of the air-film array. Symbols: dashed line, the profiles of maximum and minimum $(\overline{U}+\tilde{U})/U_e$ in one modulation cycle; dotted dash line, the mean $\overline{U}/\overline{U_e}$ profile; solid line, baseline mean $\overline{U}/U_\infty$ profile.

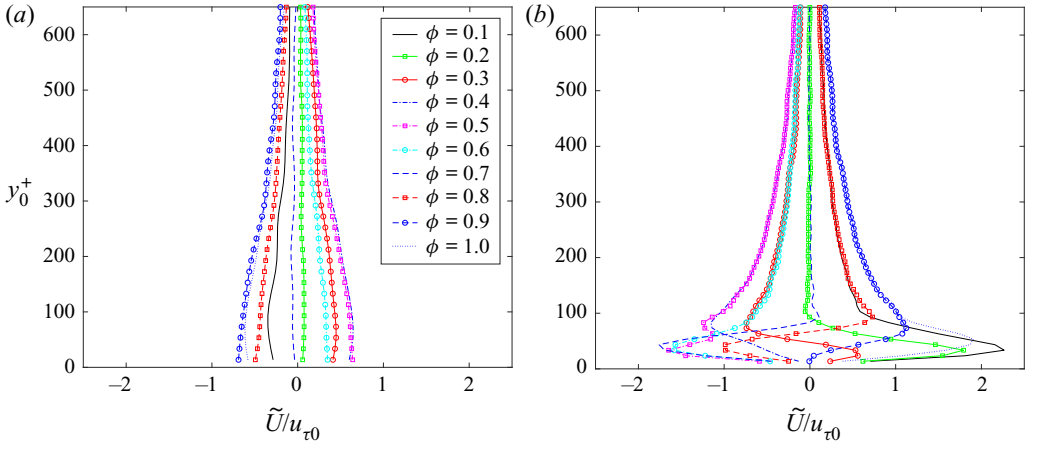


FIGURE 11. Phase-locked streamwise velocity ($\tilde{U}/u_{\tau 0}$) profiles at the (*a*) leading edge ($x_0^+ = 800$) and (*b*) trailing edge ($x_0^+ = 1550$) of the air-film array resemble the Stokes boundary layer generated by a streamwise oscillating flat plate. Information on the equally spaced phase ($\phi$) is also shown.

near-wall $\tilde{U}$ is strong at both the leading and trailing edges of the air-film array (i.e. the amplitude of $\tilde{U}$ is up to 2 $u_{\tau 0}$). However, the oscillatory motion behaves differently at the two locations. At the leading edge of the air-film array, $\tilde{U}$ oscillates in phase at all wall-normal distances (i.e. at any instant the entire $\tilde{U}$ profile resides on either the positive or negative side of the zero mean). However, at the trailing edge, $\tilde{U}$ can be either positive or negative in the same phase, depending on its distance from the wall. In the classical Stokes layer, the oscillatory velocity decays exponentially with the distance from the wall. The penetration depth ($l = \sqrt{2\nu/\omega}$) of a classical Stokes layer at 50 Hz is equal to 79 mm, which has a non-dimensional value of $lu_{\tau 0}/\nu = 1.7$. At this distance from the wall, the oscillation velocity drops to 37 % of its maximum. The current oscillatory

motion extends into regions much further away from the wall and does not seem to follow an exponential decay. Upstream of the air-film array, the peak of $\tilde{U}$ is found close to the wall; downstream of the air-film array, the maximum of $\tilde{U}$ is detected at approximately $y_0^+ = 65$. Interestingly, the maximum height of the air film (approximately $y_0^+ = 60$) is also observed at a similar wall-normal distance.

The oscillatory motion not only exists in the streamwise velocity but also in the wall-normal velocity. A more comprehensive depiction of the oscillatory motion is presented in the phase snapshot contours of $\tilde{U}$ and $\tilde{V}$ in one modulation cycle (shown in figures 12 and 13, respectively). The phase snapshots were acquired at equal time intervals from each other. The maximum height of the air film ($h_0^+$) at the corresponding phase is highlighted as shown in the plots along the right-hand side edges of the contours. The results show that $\tilde{U}$ and $\tilde{V}$ oscillate with similar amplitude (approximately $2\,u_{\tau 0}$). However, their behaviours differ considerably; $\tilde{U}$ is strong at the leading and trailing edges of the air-film array whereas $\tilde{V}$ mainly exists in the region above the air-film array. The values of $\tilde{U}$ at the leading and trailing edges are always out of phase (i.e. the sign of $\tilde{U}$ flips at the two locations) but $\tilde{V}$ is always in phase at all locations.

The phase variations of $\tilde{U}$ and $\tilde{V}$ are in line with the air-film expansion and contraction shown by the phase variation of $h_0^+$. In the phases during which the air film expands, $\tilde{U}$ is negative and positive at the leading and trailing edges of the air-film array, respectively, possibly due to the decelerating and accelerating effect of expanding air films at the two locations. In the same phases, $\tilde{V}$ is positive. The magnitude of $\tilde{V}$ reaches zero when the air film stops expanding. These observations are in harmony with the 'push' and 'pull' effect of the expansion and contraction motion of the air films.

Figure 14 shows phase snapshots of the oscillatory transverse vorticity ($\widetilde{\Omega}_z$) in the near-wall region, where $\widetilde{\Omega}_z = \partial\tilde{V}/\partial x - \partial\tilde{U}/\partial y$. The sign of $\widetilde{\Omega}_z$ periodically changes in the near region of the air-film array. Both positive and negative $\widetilde{\Omega}_z$ emerge near the wall and expand into regions away from the wall. The existing $\widetilde{\Omega}_z$ gradually diminishes as the $\widetilde{\Omega}_z$ with the opposite sign emerges. Seemingly, $\widetilde{\Omega}_z$ is repeatedly 'pushed' away from the wall.

### 4.3. *Process of streamwise momentum transfer*

In canonical flat plate TBLs, the streamwise momentum is transferred toward the wall by the Reynolds shear stress ($-\overline{u'v'}$) and imposed on the wall via the viscous shear stress ($\nu(\partial\overline{U}/\partial y)$), resulting in elevated wall skin friction. In regions away from the wall, momentum is mainly transferred by the Reynolds shear stress. In the near-wall region such as in the viscous sub-layer, the momentum is mainly transferred by the viscous shear stress (Tennekes & Lumley 1972). As shown in § 4.2, harmonic flow motions such as $\tilde{U}$ and $\tilde{V}$ are present when the air films are modulated. In this scenario, additional shear stress such as $-\tilde{U}\tilde{V}$ also participates in transferring the streamwise momentum. In this section, the shear stress distribution in the vicinity of air films is presented.

With the triply decomposed velocity field, the total shear stress ($\tau_{total}$) in regions away from the wall is expressed by the following equation:

$$\tau_{total} = -\left(\overline{U} + \tilde{U} + u'\right)\left(\overline{V} + \tilde{V} + v'\right). \tag{4.1}$$

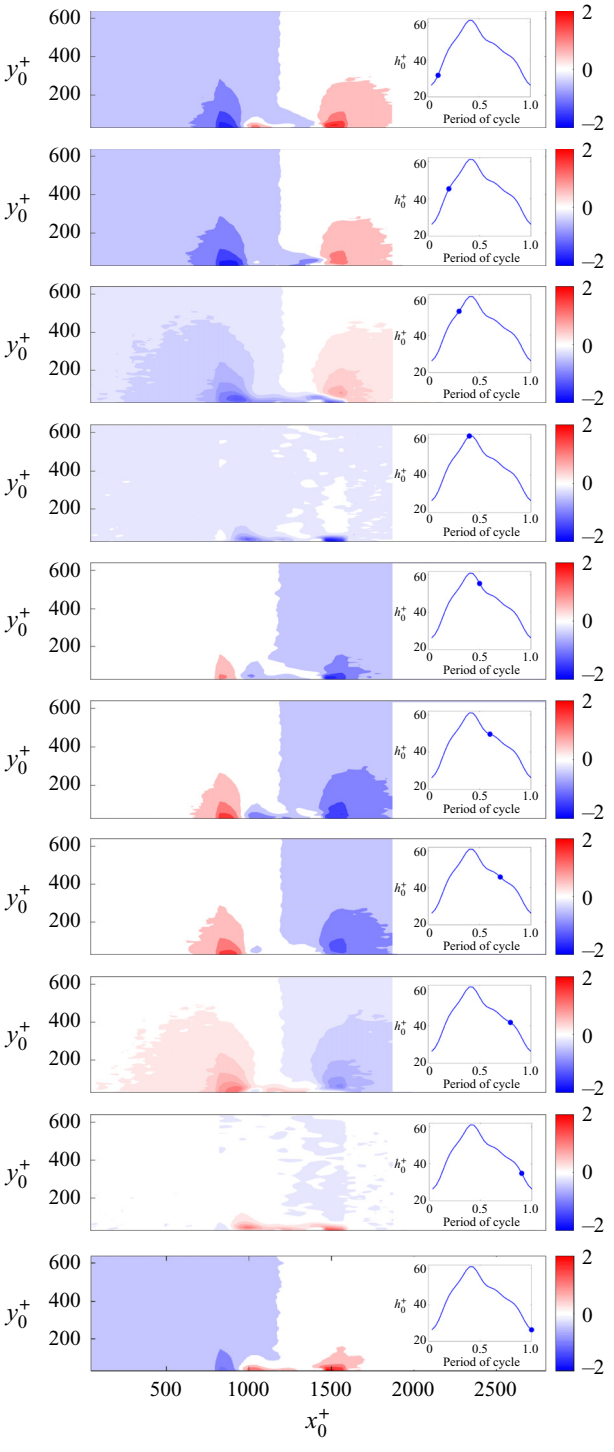


FIGURE 12. Phase snapshots for $\tilde{U}/u_{\tau 0}$ at equal time intervals in one modulation cycle. The air-film array is located between $x_0^+ = 900$ and $x_0^+ = 1500$. The maximum height of the air film ($h_0^+$) at each phase is highlighted by the markers. The behaviour of $\tilde{U}$ reflects the 'push' and 'pull' effect of the air film.

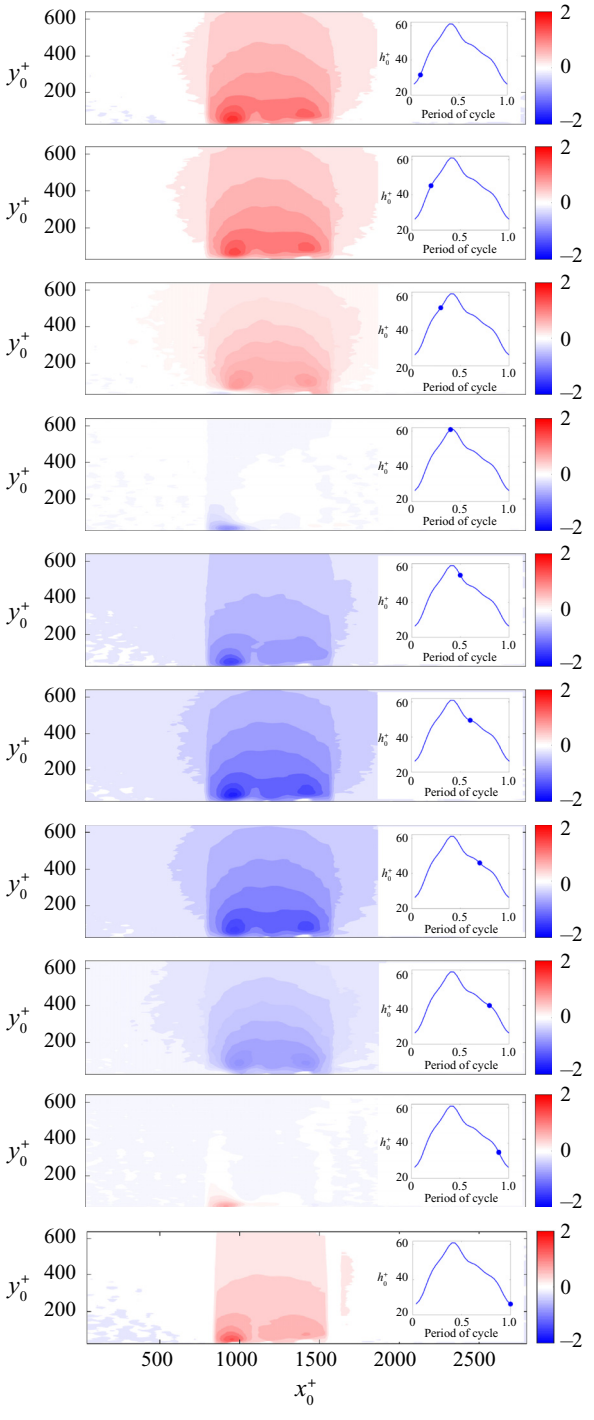


FIGURE 13. Phase snapshots for $\tilde{V}/u_{\tau 0}$ at equal time intervals in one modulation cycle. The air-film array is located between $x_0^+ = 900$ and $x_0^+ = 1500$. The maximum height of the air film ($h_0^+$) at each phase is highlighted by the markers. The behaviour of $\tilde{V}$ reflects the 'push' and 'pull' effect of the air film.

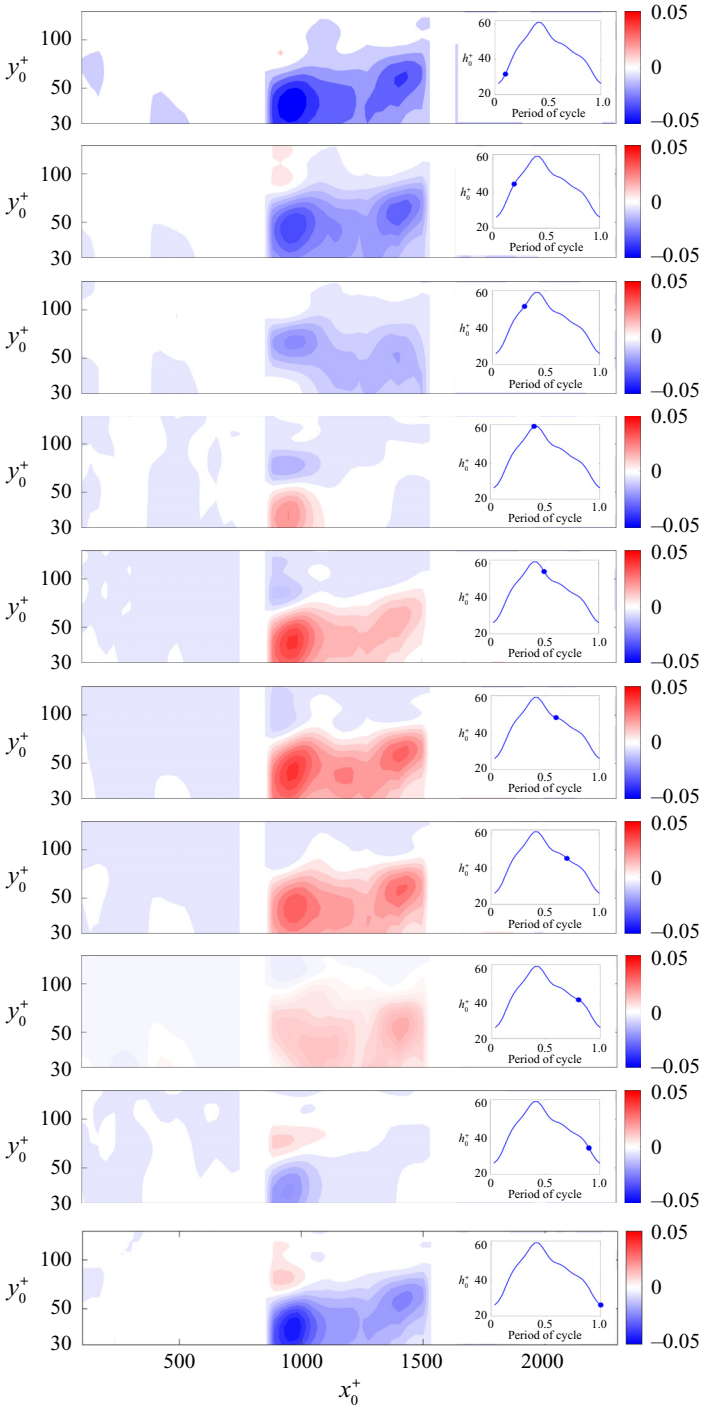


FIGURE 14. Phase snapshots of the near-wall oscillatory transverse vorticity ($\nu\widetilde{\Omega}_z/u_{\tau 0}^2$) at equal time intervals in one modulation cycle. The $y$ axis is in log scale and the air-film array is located between $x_0^+ = 900$ and $x_0^+ = 1500$. The maximum height of the air film ($h_0^+$) at each phase is highlighted by the markers.

The time-averaged total shear stress ($\overline{\tau}_{total}$) has three components, as shown in (4.2). The detailed derivation process is given in appendix A. For the purpose of convenience, the three shear stress components are henceforth referred to as the Reynolds shear stress, the wave shear stress and the mean motion shear stress, respectively.

$$\overline{\tau}_{total} = -\left(\overline{UV} + \overline{\tilde{U}\tilde{V}} + \overline{u'v'}\right). \tag{4.2}$$

Figures 15(*a*)–15(*d*) show the contour plots of these three forms of shear stress ($-\overline{u'v'}$, $-\overline{\tilde{U}\tilde{V}}$, and $-\overline{UV}$) and $\overline{\tau}_{total}$, all non-dimensionalized by $u_{\tau 0}^2$. Because the magnitude of $-\overline{UV}$ is larger than the other two shear stress components, the colour bar scales for $-\overline{u'v'}$ and $-\overline{\tilde{U}\tilde{V}}$ are set $O(1)$ smaller than those of $-\overline{UV}$ and $\overline{\tau}_{total}$. In the case of the baseline TBL, $-\overline{\tilde{U}\tilde{V}}$ does not exist and $-\overline{UV}$ is trivial. The $-\overline{u'v'}$ of the baseline case is contour plotted in figure 17 in the same colour bar scale as that in figure 15(*a*).

As shown in figure 15(*a*), the $-\overline{u'v'}$ is observed to be slightly suppressed in the region above the air-film array, i.e. at $y_0^+ \approx 75$. However, it is greatly enhanced downstream of the air-film array. The elevated $-\overline{u'v'}$ extends for approximately 3 $\delta_0$ farther downstream before relaxing to the baseline value (not shown here). The wave shear stress ($-\overline{\tilde{U}\tilde{V}}$) is shown in figure 15(*b*), which is mainly concentrated near the leading and trailing edges of the air-film array and has opposite signs at the two locations. The magnitude of $-\overline{\tilde{U}\tilde{V}}$ is comparable to that of the local Reynolds shear stress ($-\overline{u'v'}$); $-\overline{UV}$ is the largest among all the shear stress components and dominates the total shear stress ($\overline{\tau}_{total}$). The sign of $\overline{\tau}_{total}$ may change depending on the wall-normal distance. For example, over the central region of the air-film array, $\overline{\tau}_{total}$ is positive and negative in the region below and above $y_0^+ \approx 100$, respectively.

The local negative $\overline{\tau}_{total}$ shown in figure 15(*d*) acts as an agent for transferring momentum away from the wall. In the region where the sign of $\overline{\tau}_{total}$ switches, as marked by the black dotted line in figure 15(*d*), a layer of zero shear stress exists. This layer starts to grow near the leading edge of the air-film array and reaches a plateau in the region above the air-film array. Near the trailing edge of air-film array, this layer rapidly bends away from the wall. The dominance of $-\overline{UV}$ in all the shear stress components and the zero-shear-stress layer is more clearly seen in the shear stress profiles given in figure 16.

The wave shear stress ($-\overline{\tilde{U}\tilde{V}}$) does not exist in the case of passive flat and bulged air films. In these cases, the total shear stress ($-\overline{u'v'} - \overline{UV}$) is shown in figure 18. The zero-shear-stress layer, which does exist with passive bulged air film, has the form of a radial ray that emits from the air-film array. However, the zero-shear-stress layer is not detectable for passive flat air films.

In the near-wall region of TBLs, the streamwise momentum is transferred by the viscous shear stress, which peaks at the wall. Figures 19(*a*)–19(*c*) depict the profiles of viscous shear stress ($(\nu/u_{\tau 0}^2)(\partial\overline{U}/\partial y)$) in the nearby region of the air films, in addition to the baseline viscous shear stress profiles at the same locations. The locations of the profiles are shown along the top $x$-axis. In the case of a bulged air film modulated at 50 Hz (shown in figure 19*a*), the near-wall viscous shear stress increases slightly upstream of the air-film array but substantially decreases over the air-film array. In addition, the peak viscous shear stress is shifted away from the wall. Downstream of the air-film array, the viscous shear stress profile relaxes to that of the baseline case. For the passive bulged air film, the viscous shear stress profiles are similar (shown in figure 19*b*). In the case of the flat air

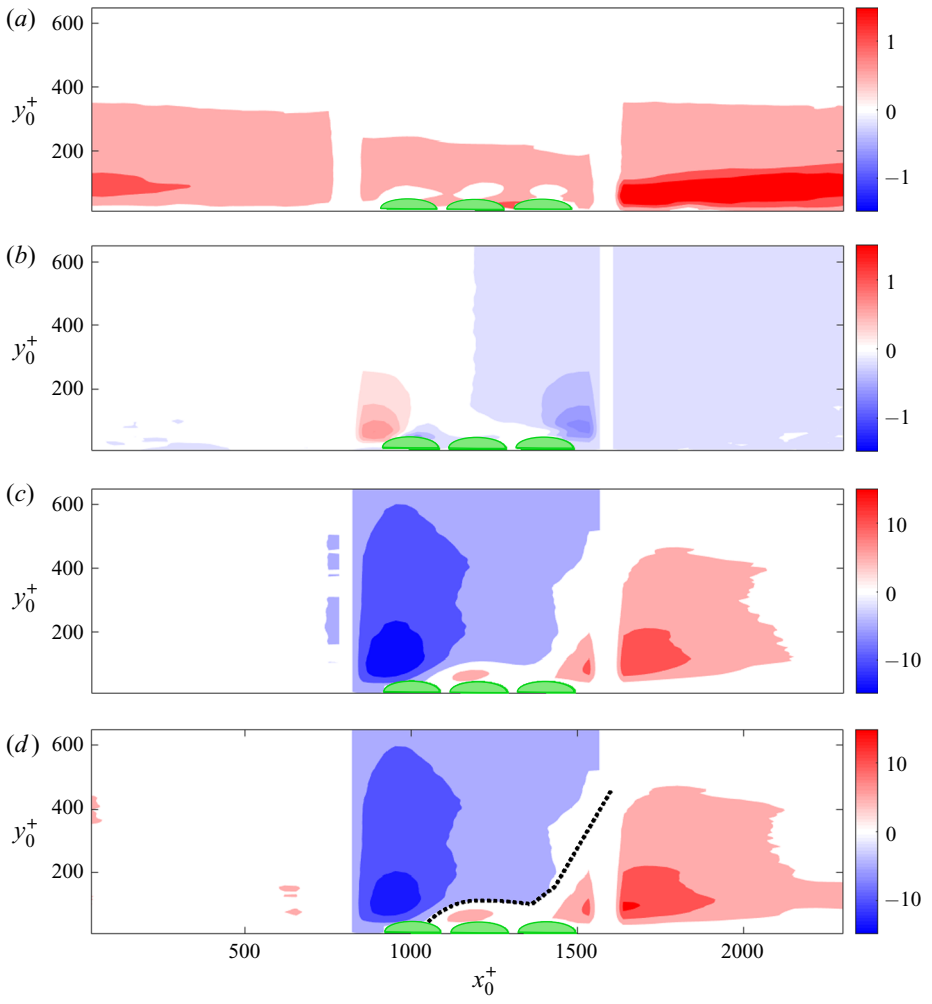


FIGURE 15. Contour plot of (*a*) Reynolds shear stress ($-\overline{u'v'}$), (*b*) mean wave shear stress ($-\overline{\tilde{U}\tilde{V}}$), (*c*) mean motion shear stress ($-\overline{UV}$) and (*d*) the sum of the above shear stresses ($\overline{\tau}_{total}$) in the presence of bulged air films modulated at 50 Hz. The air films are represented by green half-ovals along the bottom edge of the panels. The colour bar scale of (*c* , *d*) is $O(1)$ larger than that of (*a* , *b*). The dividing line for positive and negative $\overline{\tau}_{total}$ is marked by the black dotted line in (*d*).

films, however, the viscous shear stress is only slightly suppressed in the near-wall region and no peak shift is observed (shown in figure 19*c*). A comparison of the downstream region of passive and modulated bulged air film (shown in figures 19*a* and 19*b*) indicates the relaxation process of viscous shear stress is more effectively delayed by the active modulation.

### 4.4. *Quantifying the skin friction reduction effect*

Estimating the wall skin friction ($C_f$) is a challenging task for unsteady TBLs such as the one examined here. One common method is the Clauser chart method (Clauser 1954),

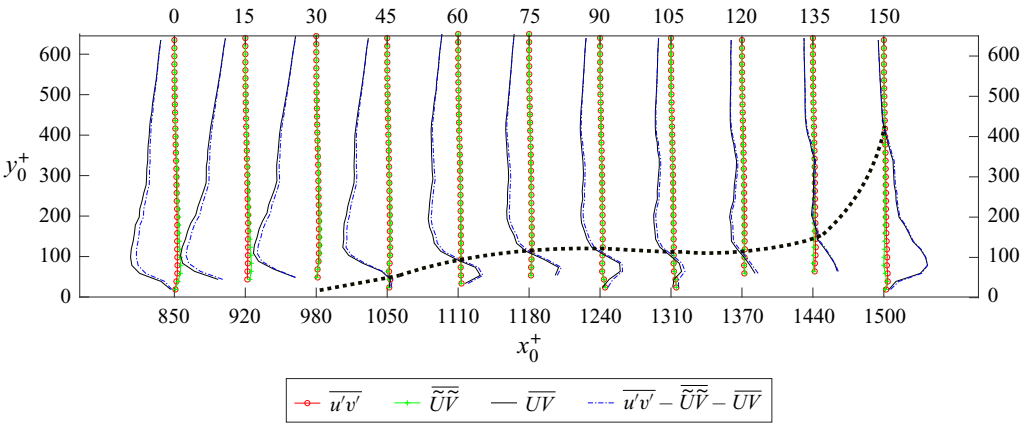


FIGURE 16. Profiles of the shear stresses shown in figure 15, with their sample locations shown along the bottom $x$-axis. Data in regions close to the air film are not included. The shear stresses are normalized by $u_{\tau 0}^2$ and are offset from each other by 15 units. The symbols for the stress components are provided in the plot. The air-film array is located between $x_0^+ = 900$ and $x_0^+ = 1500$ and the zero-shear-stress layer is marked by the black dotted line.

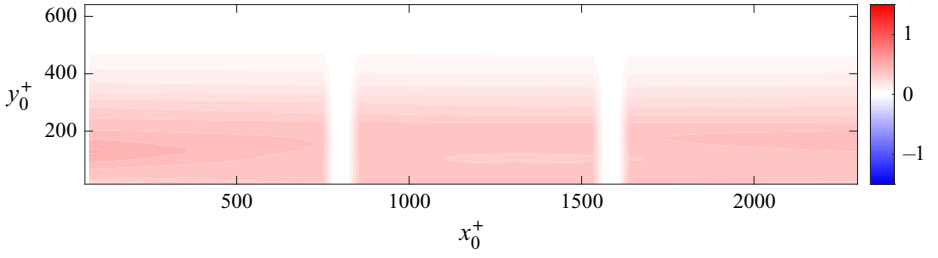


FIGURE 17. Baseline Reynolds shear stress ($-\overline{u'v'}$) with the same colour bar scale as in figure 15($a$). The baseline $-\overline{UV}$ is trivial and is not shown here.

which estimates the wall friction velocity ($u_\tau$) by fitting the log region of the velocity profile to the canonical log layer. The skin friction coefficient ($C_f$) can be further calculated using the formula $C_f = 2u_\tau^2/U_\infty^2$. Because of this feature, the Clauser chart method is only valid to estimate $C_f$ when the velocity profile has a log layer. For velocity profiles in which this layer is absent, such as those measured over the passive and modulated bulged air films (shown in figure 5), the Clauser chart method may not work. Therefore, the Clauser chart method was applied to regions sufficiently far upstream and downstream away from the air-film array, where the log-parallel layers exist in the $\overline{U}$ profile (i.e. those shown in figure 7). The Clauser chart method previously provided a good approximation of $C_f$ using the $\overline{U}$ profiles that have similar log-parallel layers, such as those in the downstream relaxation region of a backward facing step (Le, Moin & Kim 1997).

The case with modulation is used to demonstrate the versatility and robustness of the Clauser chart method. In this case, the phase-varying friction velocity is estimated using the profile of $\overline{U} + \tilde{U}$ and the corresponding skin friction coefficient ($\widetilde{C_f}$) is calculated using the phase-dependent free-streamvelocity $U_e$ defined in § 4.2. At each phase, the final portion of the velocity profile used for determining the friction velocity was between 40 $y^+$ to 0.2 $\delta$, which is within the range of the log layer (30 $y^+$ to 0.3 $\delta$) defined

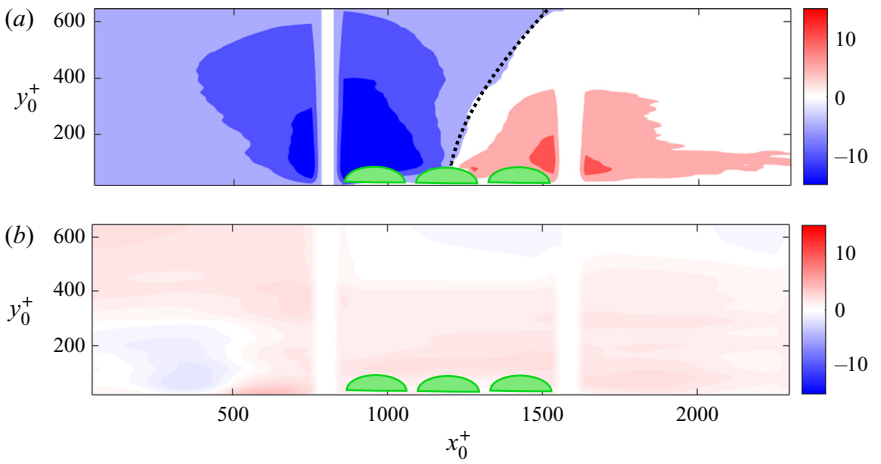


FIGURE 18. Total shear stress ($-\overline{u'v'} - \overline{UV}$) in the presence of passive (*a*) bulged and (*b*) flat air films. The air-film array is located between $x_0^+ = 900$ and $x_0^+ = 1500$. The layer of zero shear stress is observed over bulged air films (marked by the black dotted line) but not over the flat air films.

by Pope (2001). Figure 20 demonstrates the phase variation of $\widetilde{C}_f$ at four streamwise locations including both the upstream and downstream regions of the air-film array (i.e. $x_0^+ = 400, 2000, 2800, 3600$). At all four locations, $\widetilde{C}_f$ periodically oscillates and is always lower than the coefficient of the baseline case ($C_{f0}$). Upstream of the air-film array, $\widetilde{C}_f$ is only slightly reduced; however, it is substantially reduced downstream of the air-film array. The reduced $\widetilde{C}_f$ continues relaxing to $C_{f0}$ in further downstream regions.

The time-averaged skin friction coefficient ($\overline{C_f}$) can be obtained by averaging $\widetilde{C}_f$ at all phases. In addition, $\overline{C_f}$ can also be estimated using the profile of mean velocity $\overline{U}$. Figure 21 compares the two values of $\overline{C_f}$ estimated using the profiles of $\overline{U}$ and $\overline{U} + \tilde{U}$. The two estimations are almost identical, which indicates the versatility and robustness of the Clauser chart method in the current scenario.

The effect of skin friction reduction ($R_{cf}$) can be defined as the ratio of the reduced skin friction coefficient over the baseline $C_{f0}$ (i.e. $R_{cf} = (C_{f0} - \overline{C_f})/C_{f0}$). Figure 22 compares $R_{cf}$ in the presence of air films that are bulged and modulated at 50 Hz, passive bulged and passive flat. In the case of bulged air film modulated at 50 Hz, $R_{cf}$ is trivial (approximately 5 %) upstream of the air-film array but is substantial (approximately 40 %) downstream thereof. The $R_{cf}$ of the passive bulged air film increases by approximately 8 % in the upstream, and decreases by 14 % in the downstream of the air-film array. In the presence of passive flat air film, neither $C_f$ reduction nor induction is observed. For cases in which the drag reduction effect is observed, $R_{cf}$ generally decays in a monotonic manner in the regions downstream to the air-film array. However, one exception is the region immediately downstream to the passive bulged air film, i.e. the region between $x_0^+ = 1500$ and $x_0^+ = 2500$ in figure 22(*b*). In this region, $R_{cf}$ monotonically increases. A possible reason for this increase could be related to the fact that the individual air film passively oscillates in a random manner. This random movement, although it could interfere with the near-wall turbulent structures, may not introduce measurable drag reduction effect in the vicinity of the air film. The modified flow structure, however, could possibly generate a larger drag reduction effect in regions that are further downstream.

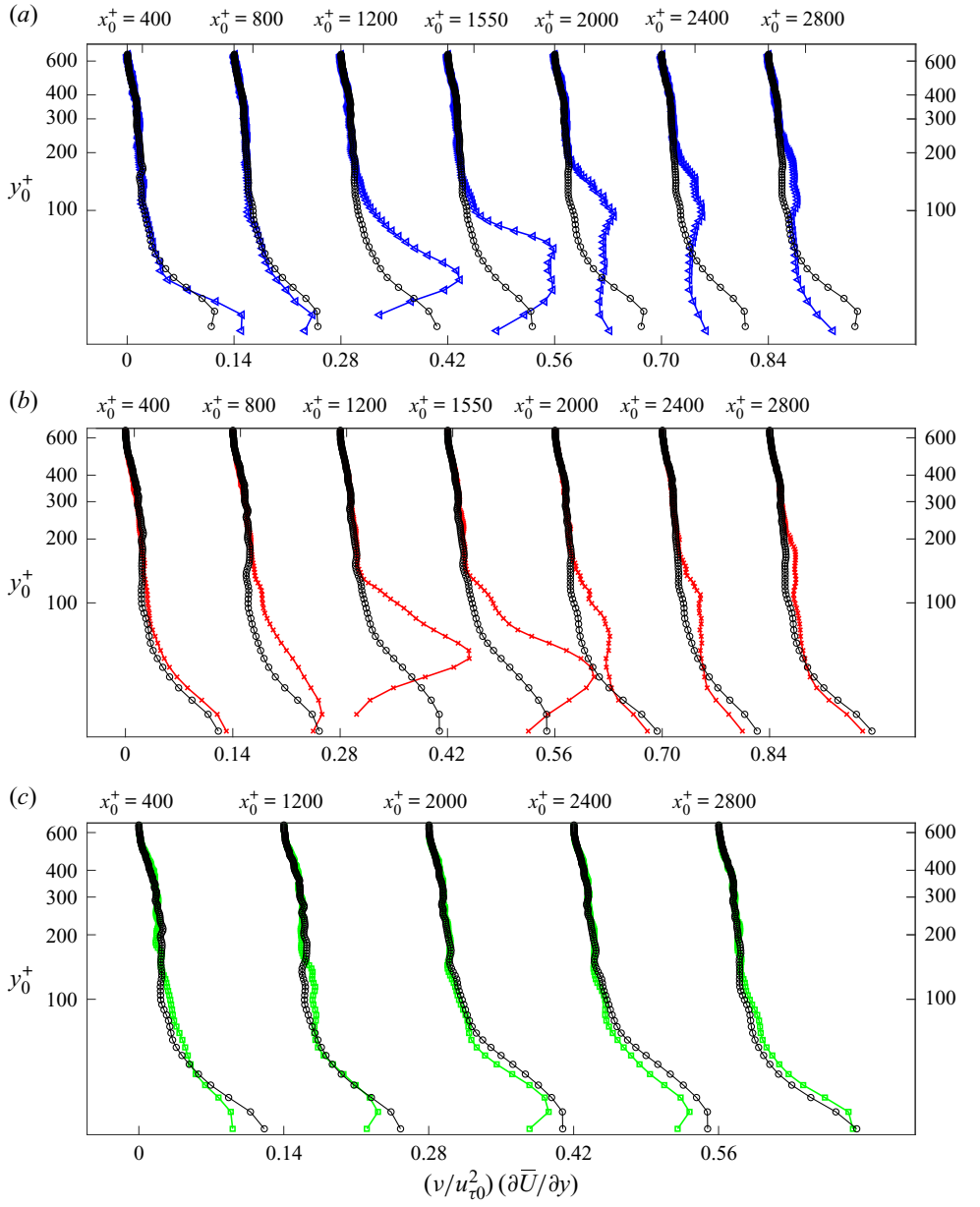


FIGURE 19. Profiles of non-dimensional viscous shear stress $((\nu/u_{\tau 0}^2)(\partial\overline{U}/\partial y))$ in the presence of (*a*) bulged air film modulated at 50 Hz, (*b*) passive bulged air film and (*c*) passive flat air film. The streamwise locations of the profiles are shown along the top $x$-axis. The air-film array is located between $x_0^+ = 900$ and $x_0^+ = 1500$. Symbols: triangles, bulged air film modulated at 50 Hz; crosses, bulged air film; squares, flat air film; black solid line, the baseline case.

Although the skin friction coefficient is significantly reduced in the downstream region of the air-film array, one valid concern is whether this effect is due to the potential form drag on the air-film array. Because the oscillating air film frequently protrudes into the

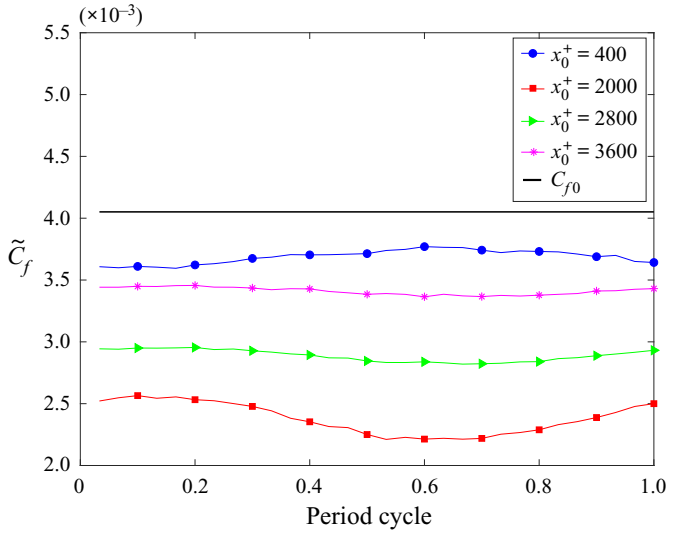


FIGURE 20. Phase-varying $\widetilde{C}_f$ at various streamwise locations in one modulation cycle. The sample locations are shown in the plot. The baseline $C_{f0}$ is also shown.

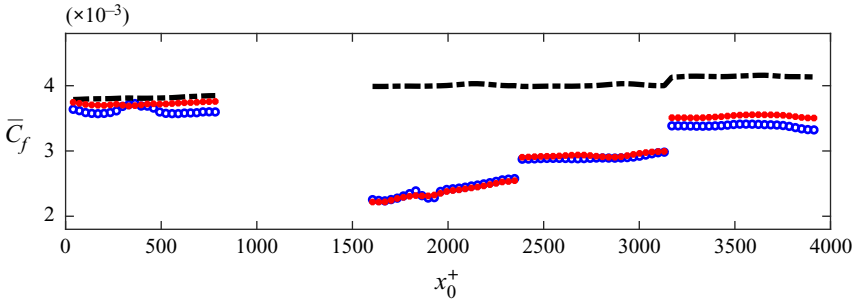


FIGURE 21. Comparison of $\overline{C_f}$ estimated using the profiles of $\overline{U} + \tilde{U}$ and $\overline{U}$. The region of air-film array (between $x_0^+ = 900$ and $x_0^+ = 1500$) is excluded from the estimation due to the absence of the log layer. Symbols: circles, time-averaged $C_f$ estimated using the $\overline{U} + \tilde{U}$ profile; triangles, $\overline{C_f}$ estimated using the $\overline{U}$ profile; dashed line, baseline TBL $C_{f0}$.

TBL, it may behave as a dynamic roughness which induces local form drag. The potential form drag effect caused by the bulged air film is investigated by replacing the air-film array with a three-dimensionally printed solid bump array that has the same geometric design (3 × 12 bumps). To mimic the shape of the fully bulged air film, each solid bump has an 8 mm square base and a maximum height of 2.5 mm (equivalent to 54 $\nu/u_{\tau 0}$). The $R_{cf}$ in the surrounding region of solid bump array is plotted in figure 23. The reduction of skin friction coefficient in the downstream region of the solid bump array was trivial (i.e. less than 3 %) and could be within the error range of Clauser chart method. This result demonstrates that the significant reduction of $C_f$ is not at the expense of form drag on bulged air films. In contrast, it is mainly due to the dynamic oscillation of the air film.

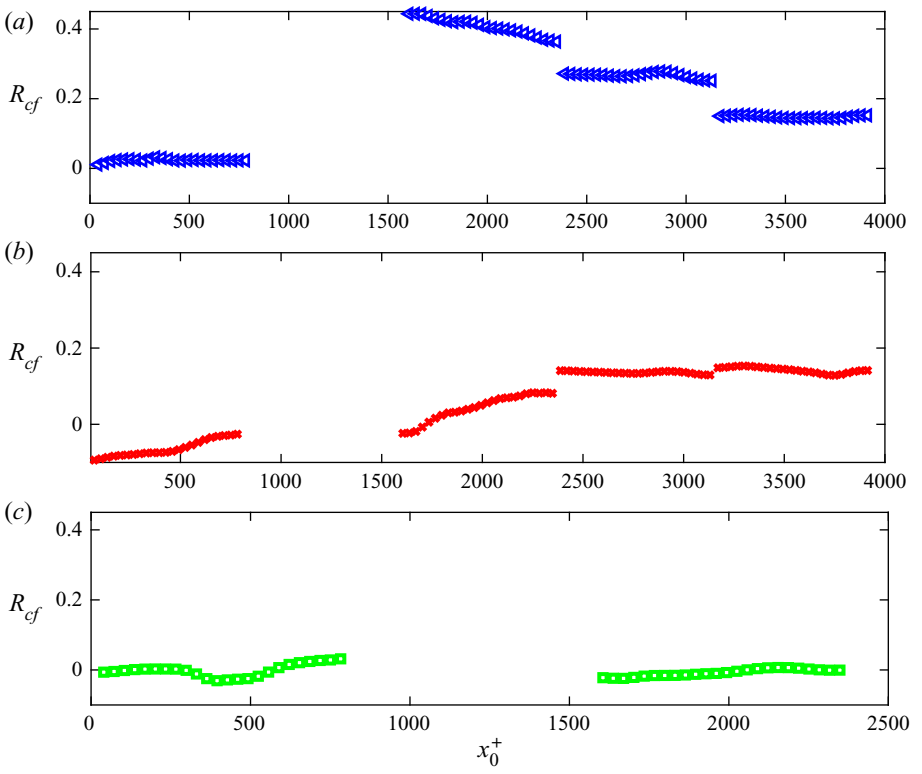


FIGURE 22. Skin friction reduction ($R_{cf}$) in the vicinity of (*a*) bulged air film modulated at 50 Hz, (*b*) passive bulged air film and (*c*) passive flat air film. The region of air-film array (between $x_0^+ = 900$ and $x_0^+ = 1500$) is excluded from the estimation due to the absence of the log layer in the velocity profiles. Symbols: triangles, bulged air film modulated at 50 Hz; crosses, bulged air film; squares, flat air film.

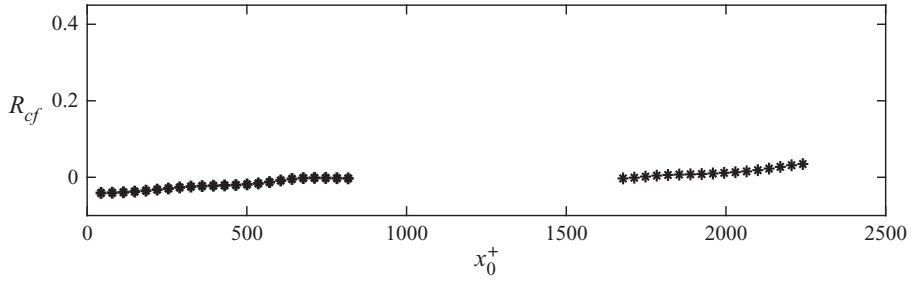


FIGURE 23. Skin friction reduction ($R_{cf}$) in the surrounding region of a solid bump array (between $x_0^+ = 900$ and $x_0^+ = 1500$) that has the same dimension as that of the air-film array. Each individual solid bump has an 8 mm square base and its maximum height is 2.5 mm (equivalent to 54 $\nu/u_{\tau 0}$).

### 4.5. *A potential mechanism for the drag reduction effect*

In this section, a control volume analysis for the streamwise momentum is presented. For a given control volume $V$, the net $x$-momentum change can be attributed to the total

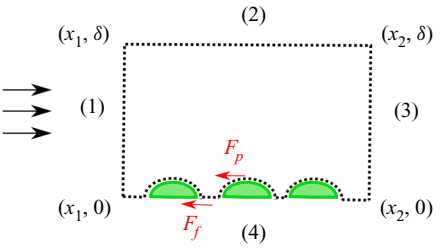


FIGURE 24. Schematic of the selected control volume. The air films are represented by the green half-oval shapes. The surface forces acting on the control volume are shown.

forces $\vec{\boldsymbol{F}}$ acting on the control surface as expressed by (4.3), where $\boldsymbol{U}$ is the velocity vector, $A$ is the boundary of the control volume and $\boldsymbol{n}$ is the outward normal vector of the boundary surface $A$. In the calculation of the time-averaged total force, only the second term (momentum-flux term) on the right-hand side of (4.3) is non-zero.

$$\boldsymbol{F} = \frac{\partial}{\partial t}\int \boldsymbol{U}\,\mathrm{d}V + \oint \boldsymbol{U}(\boldsymbol{U}\cdot\boldsymbol{n})\,\mathrm{d}A. \tag{4.3}$$

The selected control volume is shown in figure 24, which covers the entire streamwise span of the air-film array and extends from $y = 0$ to $y = \delta_0$. The surface forces that are responsible for the $x$-momentum change act along the surface (4) in figure 24, which includes the wall friction ($F_f$) as well as the dynamic force generated by the oscillating air film ($F_p$). The two surface forces will be evaluated together. With triple decomposition, the $x$-momentum flux across the surfaces (1), (2) and (3) can be derived following the derivation process of (4.2), using the phase-average properties given in appendix A. The integrated momentum flux across the three surfaces are given below:

$$\left.\begin{aligned}
\phi_1 &= -\int_0^{\delta} \overline{U^2} + \widetilde{\overline{U^2}} + \overline{u'^2}\,\mathrm{d}y|_{x=x_1},\\
\phi_3 &= \int_0^{\delta} \overline{U^2} + \widetilde{\overline{U^2}} + \overline{u'^2}\,\mathrm{d}y|_{x=x_2},\\
\phi_2 &= \int_{x_1}^{x_2} \overline{UV} + \widetilde{\overline{UV}} + \overline{u'v'}\,\mathrm{d}y|_{y=\delta_0}.
\end{aligned}\right\} \tag{4.4}$$

As such, the total force $F_f + F_p$ is equal to $\phi_1 + \phi_2 + \phi_3$, the values of which are provided in table 3. The negative values correspond to drag forces. For the baseline case, the total force is only due to wall friction. The average value of the wall skin friction coefficient ($\overline{C_f}$) is found to be equal to 0.0052, which is close to the prediction by Prandtl's $\frac{1}{7}$th law ($\overline{C_f} = 0.0047$) and the prediction by the charted Clauser method ($\overline{C_f} = 0.0041$). However, in the three cases in which the air film exists, the total forces have positive values, which suggests that positive $x$-momentum is transferred from the dynamic air film to the TBL. The most significant momentum gain is observed in the case with modulated bulged air film, the magnitude of which is more than five times larger than the magnitude of the baseline momentum loss. In contrast, in the case of solid bump, considerable increase in drag force is observed.

The above-mentioned momentum gain can be qualitatively seen in the profiles of $x$-momentum flux ($\overline{U^2} + \widetilde{\overline{U^2}} + \overline{u'^2}$) along the upstream surface (1) and the downstream

| Cases | Baseline TBL | Modulated bulged air film | Passive bulged air film | Passive flat air film | Solid bump |
|---|---|---|---|---|---|
| $\frac{F_f + F_p}{\frac{1}{2}L_0 U_\infty^2}$ | $-5.2 \times 10^{-3}$ | $+2.8 \times 10^{-2}$ | $+6.9 \times 10^{-3}$ | $+6.2 \times 10^{-3}$ | $-10.3 \times 10^{-3}$ |

TABLE 3. Total force normalized by $\frac{1}{2}L_0 U_\infty^2$ over the control volume, where $L_0$ is the streamwise span of the control volume. The negative values correspond to drag forces.

surface (3) of the control volume (shown in figure 25). In the presence of 50 Hz modulation, the downstream momentum flux is reduced in the inner region but increased in the outer region, when compared to the upstream momentum flux. A similar trend is observed for the passive bulged air film. In the downstream of a solid bump, a strong near-wall momentum deficit is observed whereas the outer layer is no different from its upstream counterpart. In the baseline case, the momentum flux is almost identical along the two surfaces.

To more clearly observe the modification in the $x$-momentum flux distribution, the profiles shown in figure 25 are offset by the baseline momentum flux along the upstream surface (1) and given in figure 26. As such, the relative momentum gain or deficit with respect to the baseline control case is reflected by the positive or negative values of the offset momentum fluxes. It is surprising to find that for all the cases with air film, even in the upstream region, the offset momentum flux has a negative and positive value in the inner and outer region, respectively. This observation suggests that the momentum deficit near the wall and the momentum gain in the outer layer already exist even before the TBL encounters the air-film array. In contrast, in the presence of solid bump, the offset momentum flux is negative across the entire boundary layer, showing a general momentum loss at different wall distances. As a reference, in the baseline case the downstream momentum flux demonstrates a trivial momentum loss. With the above-mentioned observations, we hypothesize that some form of positive $x$-momentum is pumped into the TBL via the air-film dynamics, and such effect extends into regions upstream of the air film.

The conjectured pumping process is sensitive to the air-film dynamics. In the case of 50 Hz modulation, the most significant momentum gain happens in the region close to $y_0^+ = 120$. In the case with passive bulged air film, the momentum gain is almost uniform in the region above $y_0^+ = 180$. The crossing points for the profiles of upstream/downstream momentum flux, in the cases of actuated and passive bulged air film, are at $y_0^+ = 66$ and $y_0^+ = 99$, respectively. In the case of flat air film, although the momentum increase over the air-film array is not obvious, the accumulated momentum gain in the upstream region is significant, i.e. the offset momentum flux is positive in regions above $y_0^+ = 36$.

The pumping effect matches well with the distribution of shear stress ($\overline{\tau}_{total}$). As demonstrated in § 4.3, the negative $\overline{\tau}_{total}$ injects $x$-momentum into the TBL. The negative $\overline{\tau}_{total}$ shown in figures 15 and 18 indicates that the pumping effect locally exits, with and without active modulation. When compared to the passive cases, the dynamic modulation produces a stronger pumping effect. Starting to exist from the upstream region of the air-film array, the negative $\overline{\tau}_{total}$ enhances the $x$-momentum transport, which explains why the $x$-momentum flux in figure 26 increases over the air-film array. The pumping effect

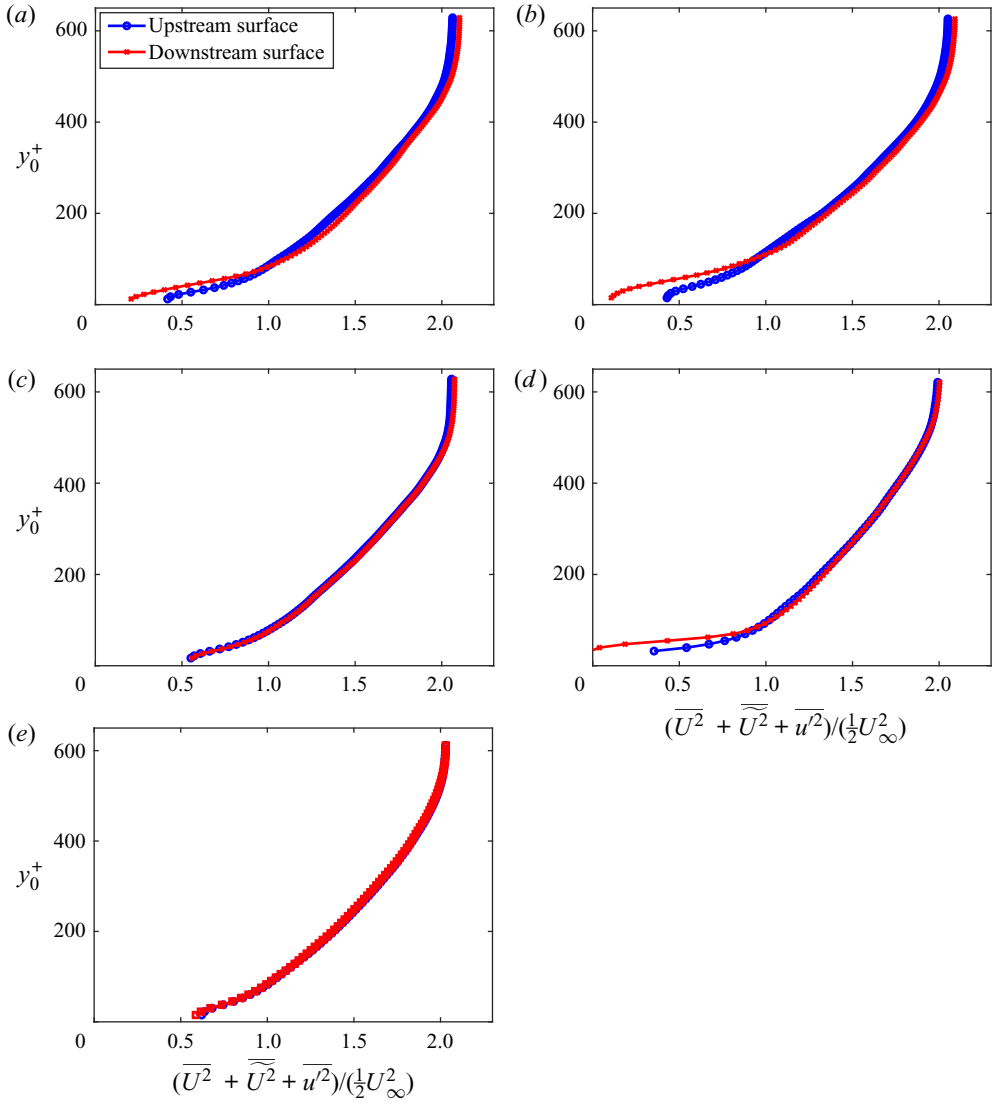


FIGURE 25. Momentum-flux distribution along the upstream and downstream surfaces of the control volume shown in figure 24. In the cases of passive and modulated bulged air film, the TBL gains $x$-momentum in the outer layer region but losses $x$-momentum in the inner layer region. The shown cases are (*a*) 50 Hz modulated air film, (*b*) passive bulged air film, (*c*) passive flat air film, (*d*) solid bump and (*e*) baseline TBL.

might be the reason for the positive $\overline{V}$ (shown in figure 8) and the outward shift of $\overline{\Omega_z}$ (shown in figure 9) as well.

As has been demonstrated by the previous research work, the pumping effect is frequently observed in successful drag reduction techniques, such as those employing controlled wall deformation or travelling-wave type blow/suction, in which sub-laminar drag and re-laminarized turbulence was observed (Min *et al.* 2006; Nakanishi, Mamori & Fukagata 2012). Hoepffner & Fukagata (2009) pointed out that 'in the context of flow control, pumping and drag reduction are strongly connected'. As such, the proposed pumping effect is likely connected to the persisting drag reduction effect in

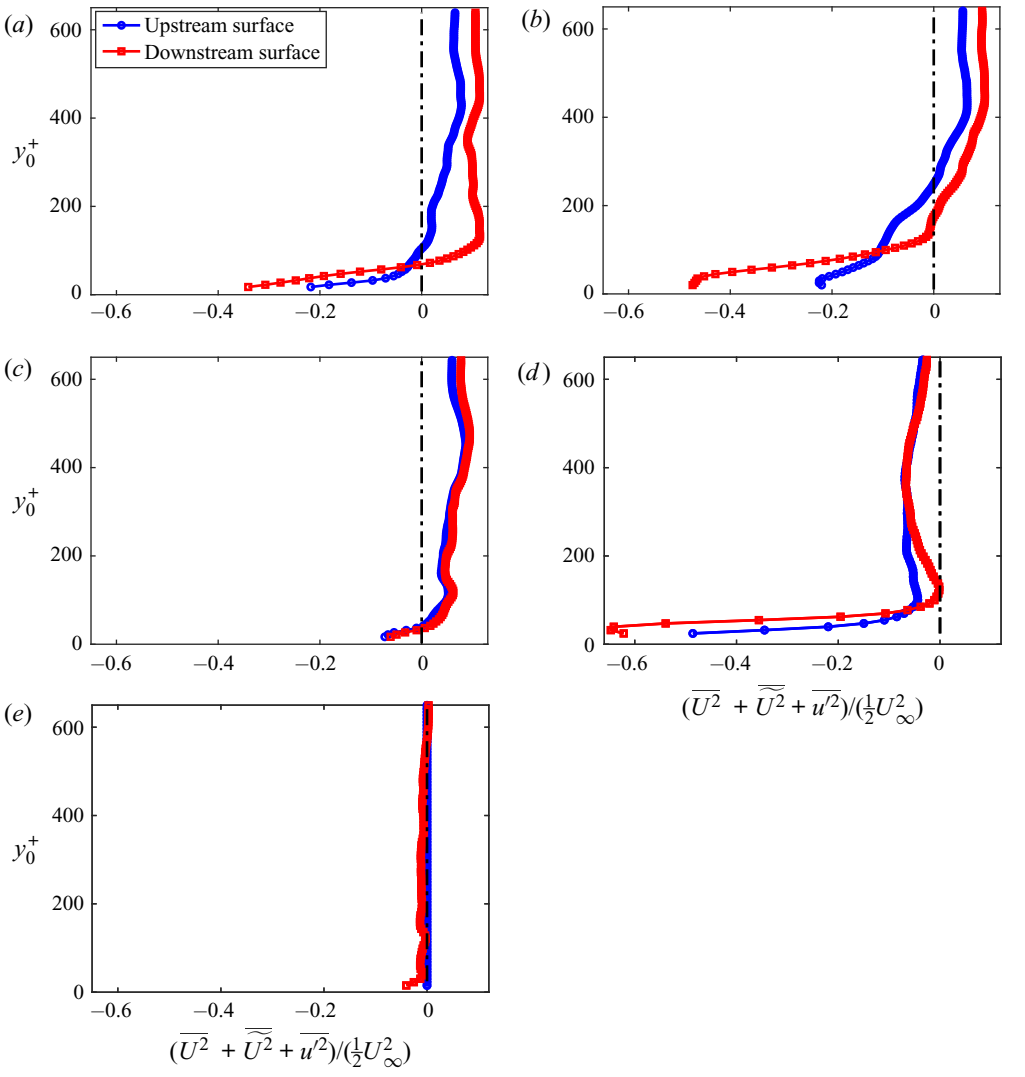


FIGURE 26. Momentum-flux profiles shown in figure 25 offset by the profile of baseline upstream momentum flux. The effect of momentum gain can be clearly observed. The shown cases are (*a*) 50 Hz modulated air film, (*b*) passive bulged air film, (*c*) passive flat air film, (*d*) solid bump and (*e*) baseline TBL.

the downstream region of air-film array (shown in figure 22). In this sense, the positive forces acting on the control volume (shown in table 3) are resulted by the combined effect of pumping and drag reduction, which cannot be clearly separated with the current investigation technique.

## 5. Discussion

### 5.1. *Connection between the flow physics and reduced wall skin friction*

The possible inter-connections between the observations presented in § 4 are critical for understanding the potential drag reduction effect. In the case with 50Hz modulation, oscillatory motion ($\tilde{U}$ and $\tilde{V}$) in the streamwise and wall-normal directions is generated

(shown in figures 12 and 13), following the 'push' and 'pull' effect of the expansion and contraction motion of the air film. In a separated DPIV measurement (results not shown here), a strong transverse oscillatory motion (i.e. $\tilde{W}$) in the side edge region of the air-film array is also observed, which could be due to the same mechanism as mentioned above. The harmonic oscillatory motions could generate harmonic vorticity field, such as the positive and negative $\widetilde{\Omega_z}$ shown in figure 14. The time-varying $\widetilde{\Omega_z}$ could interact with the $\overline{\Omega_z}$ of the existing TBL, which might result in the observed $\overline{\Omega_z}$ (shown in figure 9). The reduced near-wall viscous shear stress $((\nu/u_{\tau 0}^2)(\partial\overline{U}/\partial y))$ shown in figure 19(*a*) is a reflection of $\overline{\Omega_z}$ being 'pushed away' from the wall because $\partial\overline{U}/\partial y$ is the main constituent of $\overline{\Omega_z}$.

The distribution of the shear stresses, as presented in § 4.3, suggests suppressed momentum transfer toward the wall in the air-film occupied region. The viscous shear stress shown in figure 19 is reduced in the near-wall region over the air-film array, which suggests reduced wall shear stress. Although the stress peak is elevated, it is shifted away from the wall and is not expected to undermine the reduced wall shear stress. The total shear stress ($\overline{\tau}_{total}$) shown in figure 15(*d*) represents the $x$-momentum flux that is transported along the wall-normal direction. As such, the zero-shear-stress layer is also a zero-momentum-flux layer. This layer acts as a barrier that separates the $x$-momentum exchange on its two sides, i.e. the region below it is 'shielded' from the flux of fast $x$-momentum coming from the above, resulting in suppressed wall skin friction. The dominant contributing component for $\overline{\tau}_{total}$ is the shear stress due to the mean motion ($-\overline{UV}$), which was found to significantly reduce the wall friction in a developing TBL (Kametani & Fukagata 2011). The pumping effect proposed in § 4.5 could be the driving force for the above-mentioned observations. However, the underlying physics of the pumping mechanism remains to be studied in the future.

The region downstream of the air-film array is the relaxation region. In this region, although the elevated total shear stress $\overline{\tau}_{total}$ (shown in figure 15*d*) suggests enhanced $x$-momentum transfer toward the wall, the near-wall viscous shear stress, which exclusively determines the friction at the wall, is still much lower than that in the baseline case (shown in figure 19*a*). The relaxation of the near-wall viscous shear stress takes several $\delta_0$. In the same fashion, the skin friction coefficient ($\overline{C_f}$) relaxes in the same region (shown in figure 21). The elevated peak of viscous shear stress resides in regions away from the wall, and naturally does not impede the observed wall friction reduction.

The dynamic oscillation of the air film is critical for the skin friction reduction effect ($R_{cf}$). The oscillation amplitude needs to be large to onset the drag reduction effect. With a passive or modulated bulged air film, a large drag reduction effect is achieved. In contrast, the drag reduction effect is trivial in the cases of a static solid bump array and in the case of a passive flat air film, where either the dynamic oscillation is absent or the oscillation amplitude is too small. Meanwhile, the oscillation frequency is likely to be critical as well. In the region downstream of passive bulged air film, the viscous shear stress $((\nu/u_{\tau 0}^2)(\partial\overline{U}/\partial y))$ relaxes faster and $R_{cf}$ is weaker when compared to the case with modulation, although in both cases the air film has a similar oscillation amplitude. This difference may be related to the influence of the oscillation frequency, which can be seen in figure 4.

### 5.2. *The sustainability and controllability of the air film*

The sustainability and controllability of the wall-attached air film deserves some discussion here. Although the air film remained wall attached in all the tested cases,

at a higher Reynolds number, the air film was found to naturally oscillate at a large magnitude and can be torn out of the air pocket. In addition, the air film becomes less responsive to the modulation signal and harder to control, because the oscillation due to the turbulent fluctuations becomes dominant. As such, the sustainability and controllability of the air film depends on the relative significance of inertia force and surface tension effect governed by the Weber number ($We = \rho v_0^2 l_c/\gamma$, where $\rho$ is the density of water, $v_0$ is the characteristic velocity, $l_c$ is the characteristic length and $\gamma$ is the surface tension of water). In the current configuration, the air films are set to face downward and the buoyancy force favours the air film remaining wall attached. When the air films face upward, however, their sustainability would also depend on the ratio of the buoyancy force over the surface tension effect, which is quantified by the Bond number ($Bo = \Delta\rho g l_c^2/\gamma$, where $\Delta\rho$ is the density difference between air and water and $g$ is the gravitational acceleration, in addition to the above-mentioned symbols). By selecting the characteristic length $l_c$ to be half of the side length of the air film (i.e. 4 mm) and the characteristic velocity $v_0$ to be $\overline{U}$ in the vicinity of the bulged air film (approximately 0.1 m s$^{-1}$), we find the current Weber number and Bond number are both of $O(1)$. At a higher Reynolds number, the surface tension effect likely needs to be enhanced to sustain the wall-attached air film, which could be realized by reducing the size of the air film. A non-dimensional scaling law for the drag reduction effect would provide guidance for optimizing the geometry design of air film and the strategy for drag control. A more comprehensive study would be necessary in future to obtain such a scaling law.

### 5.3. *Connection with other drag reduction techniques*

The current drag reduction technique appears to be primarily driven by the dynamic oscillation of the air film rather than the 'slip-flow' effect, even though the effect of dynamic oscillation could be amplified by the slip surface. Many active flow control techniques that have successfully generated drag reduction effect show some overlap with the current technique. For example, active forcing techniques, such as those utilizing periodic blow/suction or a synthetic jet, could reduce the turbulent drag by as much as 40 % (Kasagi, Suzuki & Fukagata 2009). On the other hand, a transversely oscillating the solid boundary could interfere with the near-wall vortical structures and reduce drag by10 %–40 % (Jung, Mangiavacchi & Akhavan 1992; Choi, DeBisschop & Clayton 1998; Karniadakis & Choi 2003). Drag reduction in the above-mentioned techniques is generally accompanied by the near-wall vortical structures being shifted away from the wall. As mentioned earlier in this section, strong transverse oscillatory motion was observed at the side edge regions of the air-film array. The flow in those regions is expected to share many similarities with the flow over a transversely actuated flat plate.

Another category of drag control methods involves employing compliant surfaces to mimic the skin of fast swimmers, such as dolphins (Kramer 1962; Choi *et al.* 1997; Gad-el Hak 2002). Over compliant coatings, which constitute various elastic materials, drag reduction of 7 %–60 % was reported. However, the drag reduction mechanism is still unclear. The air film in the current technique is essentially an extremely compliant elastic surface that allows 'slip flow' on top. As such, the current technique may share some similarities with the compliant surface methods. Furthermore, the actuated compliant surface can pump flow forward, such as in the case of impedance pump (Rinderknecht, Hickerson & Gharib 2005). In this regard, the connection to either passive or actuated compliant surface may shed light on the mechanisms of the current technique.

## 6. Conclusions

This study demonstrates that the near-wall TBL can be effectively manipulated by dynamically modulating wall-attached air films, which essentially generate a dynamic slip boundary condition. In the vicinity of the modulated air films, the near-wall TBL demonstrates harmonic flow motions similar to the Stokes boundary layer. The observation of a zero-shear-stress layer and reduced near-wall viscous shear stress suggests that the momentum transferred towards the wall is reduced in the air-film region. Estimated by the Clauser chart method, the wall skin friction is substantially reduced in the downstream region of the oscillating air films. In the air-film region, a pumping effect that injects positive $x$-momentum into the outer layer of the TBL seems to exist. The injected $x$-momentum might be connected to the outward shift of the near-wall vortical structures and the suppression of wall skin friction. This proposed mechanism still needs to be verified by future investigations.

Although the results show a promising mechanism and a large skin friction reduction effect, applying the demonstrated air-film system for manipulating TBL at a higher Reynolds number still needs to be tested. Apart from this, the actual energy saving may be compromised by the energy consumed in achieving active modulation. In the future, the physical mechanism behind the air-film dynamic oscillation and how the oscillation would interfere the surrounding vorticity field will be investigated. The understanding of such mechanisms could facilitate understanding of the observed pumping effect and help in the development of efficient turbulent drag reduction techniques.

## Acknowledgements

This work was supported by the Office of Naval Research under grant no. N00014-15-1-2479. C.W. was supported by the Stanback fellowship at GALCIT, Caltech. The authors appreciate the communication and discussion with Professor G.L. Brown.

## Declaration of interests

The authors report no conflict of interest.

## Appendix A. Derivation of time-averaged shear stress with triple decomposition

For a given signal $f$ that is triple decomposed as $f = \overline{F} + \tilde{F} + f'$, the following identities automatically hold:

$$\overline{\tilde{F}} = \overline{f'} = \tilde{f'} = 0. \tag{A 1}$$

Based on these identities, in the presence of two independent variables $f$ and $g$ that are triply decomposed, the following equations automatically hold, where $\langle\cdot\rangle$ and $\bar{\cdot}$ represents the phase-averaged and time-averaged quantities, respectively,

$$\langle\tilde{F}G\rangle = \tilde{F}\langle G\rangle, \quad \langle\overline{F}G\rangle = \overline{F}\langle G\rangle, \quad \overline{\left\langle\tilde{F}g'\right\rangle} = \overline{\tilde{F}g'} = 0. \tag{A 2a–c}$$

Applying the above properties to the $u$ and $v$ velocities, the following products are equal to zero:

$$\overline{\overline{U}v'} = \overline{\overline{V}u'} = \overline{\overline{U}\tilde{V}} = \overline{\overline{V}\tilde{U}} = \overline{\tilde{U}v'} = \overline{\tilde{V}u'} = 0. \tag{A 3}$$

Therefore, expanding (4.1) and taking the time average, we obtain the expression shown in (4.2).

## REFERENCES


BATCHELOR, G. K. 2000 *An Introduction to Fluid Dynamics*. Cambridge University Press, p. 635.

BIDKAR, R. A., LEBLANC, L., KULKARNI, A. J., BAHADUR, V., CECCIO, S. L. & PERLIN, M. 2014 Skin-friction drag reduction in the turbulent regime using random-textured hydrophobic surfaces. *Phys. Fluids* **26** (8), 085108.

CECCIO, S. L. 2010 Friction drag reduction of external flows with bubble and gas injection. *Annu. Rev. Fluid Mech.* **42**, 183–203.

CHOI, C.-H. & KIM, C.-J. 2006 Large slip of aqueous liquid flow over a nanoengineered superhydrophobic surface. *Phys. Rev. Lett.* **96** (6), 066001.

CHOI, K.-S., DEBISSCHOP, J.-R. & CLAYTON, B. R. 1998 Turbulent boundary-layer control by means of spanwise-wall oscillation. *AIAA J.* **36** (7), 1157–1163.

CHOI, K.-S., YANG, X., CLAYTON, B. R., GLOVER, E. J., ATLAR, M., SEMENOV, B. N. & KULIK, V. M. 1997 Turbulent drag reduction using compliant surfaces. *Proc. R. Soc. Lond.* A **453** (1965), 2229–2240.

CLAUSER, F. H. 1954 Turbulent boundary layers in adverse pressure gradients. *J. Aeronaut. Sci.* **21** (2), 91–108.

DE GRAAFF, D. B. & EATON, J. K. 2000 Reynolds-number scaling of the flat-plate turbulent boundary layer. *J. Fluid Mech.* **422**, 319–346.

FUKUDA, K., TOKUNAGA, J., NOBUNAGA, T., NAKATANI, T., IWASAKI, T. & KUNITAKE, Y. 2000 Frictional drag reduction with air lubricant over a super-water-repellent surface. *J. Mar. Sci. Technol.* **5** (3), 123–130.

GOLOVIN, K. B., GOSE, J. W., PERLIN, M., CECCIO, S. L. & TUTEJA, A. 2016 Bioinspired surfaces for turbulent drag reduction. *Phil. Trans. R. Soc.* A **374** (2073), 20160189.

GAD-EL HAK, M. 2002 Compliant coatings for drag reduction. *Prog. Aerosp. Sci.* **38** (1), 77–99.

HOEPFFNER, J. & FUKAGATA, K. 2009 Pumping or drag reduction?. *J. Fluid Mech.* **635**, 171–187.

HUSSAIN, A. K. M. F. & REYNOLDS, W. C. 1970 The mechanics of an organized wave in turbulent shear flow. *J. Fluid Mech.* **41** (2), 241–258.

JIMÉNEZ, J. & PINELLI, A. 1999 The autonomous cycle of near-wall turbulence. *J. Fluid Mech.* **389**, 335–359.

JUNG, W.-J., MANGIAVACCHI, N. & AKHAVAN, R. 1992 Suppression of turbulence in wall-bounded flows by high-frequency spanwise oscillations. *Phys. Fluids* A **4** (8), 1605–1607.

KAMETANI, Y. & FUKAGATA, K. 2011 Direct numerical simulation of spatially developing turbulent boundary layers with uniform blowing or suction. *J. Fluid Mech.* **681**, 154–172.

KARNIADAKIS, G. E. & CHOI, K.-S. 2003 Mechanisms on transverse motions in turbulent wall flows. *Annu. Rev. Fluid Mech.* **35** (1), 45–62.

KASAGI, N., SUZUKI, Y. & FUKAGATA, K. 2009 Microelectromechanical systems–based feedback control of turbulence for skin friction reduction. *Annu. Rev. Fluid Mech.* **41**, 231–251.

KRAMER, M. O. 1962 Boundary layer stabilization by distributed damping. *Naval Engrs J.* **74** (2), 341–348.

LE, H., MOIN, P. & KIM, J. 1997 Direct numerical simulation of turbulent flow over a backward-facing step. *J. Fluid Mech.* **330**, 349–374.

LING, H., SRINIVASAN, S., GOLOVIN, K., MCKINLEY, G. H., TUTEJA, A. & KATZ, J. 2016 High-resolution velocity measurement in the inner part of turbulent boundary layers over super-hydrophobic surfaces. *J. Fluid Mech.* **801**, 670–703.

MIN, T., KANG, S. M., SPEYER, J. L. & KIM, J. 2006 Sustained sub-laminar drag in a fully developed channel flow. *J. Fluid Mech.* **558**, 309–318.

NAKANISHI, R., MAMORI, H. & FUKAGATA, K. 2012 Relaminarization of turbulent channel flow using traveling wave-like wall deformation. *Intl J. Heat Fluid Flow* **35**, 152–159.

POPE, S. B. 2001 *Turbulent Flows*. Cambridge University Press.

RASTEGARI, A. & AKHAVAN, R. 2015 On the mechanism of turbulent drag reduction with super-hydrophobic surfaces. *J. Fluid Mech.* **773**, R4.

RINDERKNECHT, D., HICKERSON, A. I. & GHARIB, M. 2005 A valveless micro impedance pump driven by electromagnetic actuation. *J. Micromech. Microengng* **15** (4), 861.

ROSENBERG, B. J., VAN BUREN, T., FU, M. K. & SMITS, A. J. 2016 Turbulent drag reduction over air-and liquid-impregnated surfaces. *Phys. Fluids* **28** (1), 015103.

ROTHSTEIN, J. P. 2010 Slip on superhydrophobic surfaces. *Annu. Rev. Fluid Mech.* **42**, 89–109.

SEO, J., GARCÍA-MAYORAL, R. & MANI, A. 2015 Pressure fluctuations and interfacial robustness in turbulent flows over superhydrophobic surfaces. *J. Fluid Mech.* **783**, 448–473.

SEO, J. & MANI, A. 2016 On the scaling of the slip velocity in turbulent flows over superhydrophobic surfaces. *Phys. Fluids* **28** (2), 025110.

TENNEKES, H. & LUMLEY, J. L. 1972 *A First Course in Turbulence*. MIT.

WANG, C. 2019 On the manipulation of a turbulent boundary layer by unsteady boundary conditions. PhD thesis, California Institute of Technology.

WHITE, C. M. & MUNGAL, M. G. 2008 Mechanics and prediction of turbulent drag reduction with polymer additives. *Annu. Rev. Fluid Mech.* **40**, 235–256.